

1 **TCSEIS-1D: An Interactive 1D Code for temperature and**  
2 **composition modelling of the crust and mantle from seismological**  
3 **data**

4  
5 Mariano S. Arnaiz-Rodríguez <sup>1\*,2</sup>, Javier Fullea <sup>1,3</sup>

6 <sup>1</sup> Department of Physics of the Earth and Astrophysics, Universidad Complutense de Madrid (UCM), Madrid 28040,  
7 Spain.

8 <sup>2</sup> Institut de Physique du Globe de Paris, Université de Paris UMR 7154, CNRS, F-75005 Paris, France

9 <sup>3</sup> Geophysics section, Dublin Institute for Advanced Studies, Dublin, Ireland

10 *Correspondence to:* Mariano S. Arnaiz-Rodríguez (mararnai@ucm.es)

11 **Contact:** Mariano S. Arnaiz-Rodríguez (mararnai@ucm.es)

12 **Abstract:** We present TCSEIS-1D, a software to model the Earth's thermochemical and geophysical structure from the  
13 surface down to the core-mantle boundary (CMB). The code is designed to estimate geophysical parameters of the Earth's  
14 crust and mantle from petrological and thermal information within a thermodynamically consistent framework and to  
15 perform forward 1D coupled geophysical-petrological modelling of the structure of the Earth. Developed in Julia  
16 Language, the open-source code is intended to be an easy-to-use, flexible, and fast. TCSEIS-1D includes tools to exploit  
17 the large repertoire of 1D seismological data available, namely: surface wave dispersion curves (of fundamental and  
18 higher modes of Rayleigh and Love waves) and receiver functions (of P, S, and SKS waves). Surface heat flow and  
19 isostatic topography can also be modelled. Four simple examples that illustrate the capabilities of the code are presented  
20 to show the sensitivity of Rayleigh wave phase velocity curves and P-to-S receiver functions to compositional and  
21 temperature variations.

Formatted: French

Formatted: Spanish

Formatted: Spanish

Formatted: Spanish

Formatted: Spanish

Formatted: English (US)

31

## 32 1 Introduction

33 The interpretation of geophysical data is a complex process that involves the quantitative treatment of measurements in  
34 order to retrieve information (presented as models or images) describing the Earth's inner structure (e.g., Aki et al., 1977;  
35 Dziewonski and Anderson, 1981; Telford et al., 1990; Grand, 2002; Rawlinson and Sambridge, 2003; Shapiro et al.,  
36 2005; Schaeffer and Lebedev, 2013; Fullea et al., 2021). The complexity and reliability of any geophysical model depend  
37 extensively on the nature (and quality) of the data selected for its characterization (e.g., Mosegaard & Tarantola, 1997;  
38 Bosch, 1999). For example, single-station P-to-S receiver functions analysis can be used to infer the depth of the Moho  
39 discontinuity and the average Vp/Vs relationship for all the crust (e.g., Zhu and Kanamori, 2000; Niu and James, 2002),  
40 while surface wave dispersion measurements are suitable to image the shear-wave velocity structure of a region via  
41 inversion (e.g., Brune and Dorman, 1963; Yanovskaya et al., 1998; Priestley and McKenzie, 2006; Lebedev et al., 2009).  
42 Each one of these examples is largely limited by the sensitivity, resolution, and noise inherent to every individual data  
43 type. Receiver functions are sensitive to the depth of sharp acoustic interfaces (but can only resolve velocity contrast and  
44 not absolute velocities), whereas surface waves are sensitive to shear wave velocity gradients (with comparatively smaller  
45 sensitivity to interfaces, e.g., Julià et al., 2000). In order to overcome their individual limitations, both receiver functions  
46 and surface waves can be jointly inverted or modeled to study the lithospheric structure under a single seismological  
47 station (e.g., Julià et al., 2000; Tkalčić et al., 2012; Calò et al., 2016; Levin et al., 2023).

48 The integration of different data sets generally requires relationships between all the quantitative variables (physical  
49 properties) involved in the various forward problems. On the one hand, some of them can be relatively easily connected,  
50 like crustal compressional wave velocity (Vp) and density ( $\rho$ ), for which several empirical formulas exist based on  
51 extensive databases (e.g., Ludwig et al., 1970; Christensen and Mooney, 1995; Godfrey et al., 1997; Brocher, 2005). On  
52 the other hand, other parameters like attenuation (Qp, Qs) or the relationship between shear wave velocity (Vs) and  
53 density ( $\rho$ ) are comparatively more difficult to correlate. Although it is tempting to assume that all properties can be  
54 correlated by simple equations (e.g. a simple polynomial formulation cf. Bosch (1999)) or that some may be discarded  
55 (e.g., the assumption of elastic wave propagation), the reality is that it is more accurate to describe them with a probability  
56 density function within an integrated framework.

57 One effective approach to overcoming this issue is to estimate the required parameters directly from the  
58 petrological composition and the in-situ temperature and pressure conditions. For instance, density ( $\rho$ ) and wave speeds  
59 (Vp and Vs) can be estimated from the rock's composition ( $\mathcal{C}$ ), temperature ( $\mathcal{T}$ ) and pressure ( $\mathcal{P}$ ). Furthermore, as  
60 porosity and fluids can have a strong effect on these values at upper crustal levels corrections must be applied (e.g., Athy,  
61 1930). Therefore, instead of trying to "guess" what an appropriate value for one master property would be, and then  
62 compute all others in relation to it (e.g., Jacobsen et al., 2008; Arnaiz-Rodríguez et al., 2021), it is more advantageous  
63 and consistent to estimate all parameters directly from the Temperature-Pressure-Rock Composition triad ( $\mathcal{TPC}$ ). In this  
64 way, we turn the "plural geophysical data" problem into the "lithology estimation" one, as named by Bosch (1999). The  
65 integrated geophysical-petrological strategy, as shown by many previous works (e.g., Afonso et al., 2008; Fullea et al.,  
66 2009; Khan et al., 2009; Munch et al., 2018; Bissig et al., 2021; Munch et al., 2021; Fullea et al., 2021), yields  
67 thermochemical results more straightforwardly interpreted into geological terms than classical —purely geophysical—  
68 approaches. Here, we present TCSEIS-1D (Temperature and Composition SEIsmological-1D), a simple forward code to  
69 model the thermal and compositional structure of the crust and mantle down to the core-mantle boundary (CMB) primarily  
70 from seismological data, i.e., Rayleigh and Love dispersion curves (group and phase velocity curves) and several types  
71 of elastic and isotropic receiver functions (the standard P-to-S as well as S-to-P and SKS-to-P). Available codes

Deleted:

Deleted: .

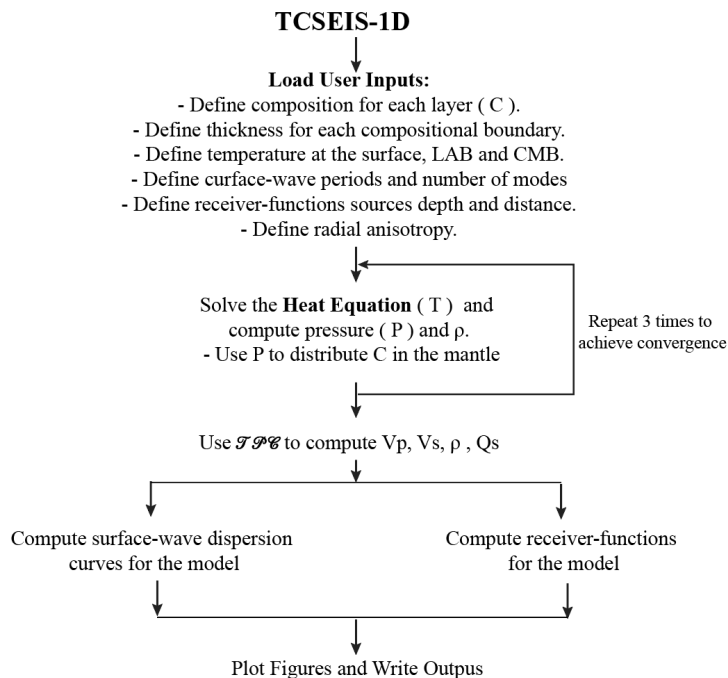
74 implementing an integrated geophysical-petrological modelling approach (either forward modelling or inversion) are  
75 mostly restricted to the lithosphere/upper mantle and do not include a lithological parametrization of the crust (e.g.,  
76 Afonso et al., 2008, Fullea et al., 2009, Afonso et al., 2013a,b; Fullea et al., 2021).  
77 TCSEIS-1D is implemented in Julia Language (Bezanson et al., 2017) for diverse reasons: it is widely used in the  
78 scientific community, flexible, open source, efficient, and has cross-platform compatibility, among others. Although Julia  
79 is still considered the "new" scientific language, it is actively used in geodesy, geostatistics, and seismology (e.g., Joshua  
80 et al., 2020; Xu et al., 2020; Zhu et al., 2022), and it is rapidly spreading across different disciplines (e.g., Dinari et al.,  
81 2019; Gao et al., 2020). Among its most notable features are: i) fast execution time (generally approaching C or Fortran-  
82 like performance); ii) dynamic typing, debugging, and syntax correction (much like Matlab or Python); iii)  
83 interoperability (it makes it easy to integrate codes from C, Python, Fortran, R, Matlab, etc.); iv) geared toward scientific  
84 computing; multiple dispatch (multiple methods in the same function for different input arguments); v) powerful parallel  
85 computing and GPU capabilities.

86 TCSEIS-1D can be employed to: (a) test geophysical models in the *JPC* model space; (b) estimate a possible  
87 solution to the composition and thermal structure of the Earth's main layers (limited by the resolution, quality, and  
88 sensitivity of the input data), (c) link velocities and density variations to *JPC* variations. After introducing the equations  
89 and assumptions that drive TCSEIS-1D's engine, the general framework of the code is presented, as well as the validation  
90 (against other codes) of the different sections that make up the software package. Finally, a few examples are presented  
91 to showcase the functionality and applicability of TCSEIS-1D with a suggestion of additional work for future versions.

92 A general flowchart of the current version of TCSEIS-1D is provided in Fig 1.

Formatted: English (US)

Formatted: English (US)



95 **Figure 1. Schematic workflow of the TCSEIS-1D algorithm. User-defined inputs include layer composition, thickness of**  
 96 **compositional boundaries, temperature at the surface, LAB and CMB, surface-wave periods and number of modes, receiver-**  
 97 **function source depth and epicentral distance, and radial anisotropy. The code iteratively solves the heat equation to obtain**  
 98 **the temperature profile, from which pressure and density are computed and used to redistribute mantle composition until**  
 99 **convergence is achieved. Thermodynamic properties are then used to calculate seismic velocities (Vp, Vs), density (rho), and**  
 100 **attenuation (Qs). The final 1-D model is used to compute surface-wave dispersion curves and receiver functions, followed by**  
 101 **visualization and output of all model results.**

Deleted: Figure. 1. TCSEIS Flowchart.

Deleted: ¶

## 105 2. Methods and Considerations

106 Mechanical properties of rocks, specifically compressional wave-speed (Vp), shear wave-speed (Vs), and  
 107 density (rho), vary in a wide range. Even though there are some clear trends in their behaviour (e.g., sedimentary rocks tend  
 108 to have lower density than igneous rocks; or mafic rocks have higher Vp than felsic rocks; e.g. Telford et al., 1990;  
 109 Brocher, 2005), a large degree of overlap exists. For example, a crustal rock with Vp=6.05 km/s can represent a very old  
 110 and consolidated carbonatic rock (i.e., a dolomite) or a felsic rock rich in quartz (i.e., a greisen). The consideration of  
 111 metamorphic rocks affected by, for example, metastability (i.e., departure from thermodynamic equilibrium) makes this  
 112 statement even more complex, as these rocks tend to show properties different from those associated with their protoliths  
 113 (e.g., Telford et al., 1990).

Deleted: than

Deleted: its protoliths

114 Seismic velocities and density of Earth's rocks depend on several parameters, namely: temperature, pressure,  
 115 mineral composition, melt fraction, fluids, and, in the case of crustal rocks, porosity and pore fluids (e.g., Christensen and

120 Mooney, 1995; Brocher, 2005). This complex mixture yields the perfect recipe for the overlap of geophysical parameter  
121 values for different rock types and geological settings as usually reported (e.g., Telford et al., 1990; Brocher, 2005). For  
122 our purpose of modeling geophysical data using petrological and thermal parameters, it is cardinal to reduce the number  
123 of free variables while keeping, at the same time, a flexible enough parameterization to represent the Earth's complexity.  
124 In this study, for the crust, we chose several ternary diagrams to classify igneous and sedimentary rocks based on  
125 mineralogical composition (Streckeisen, 1974; Le Bas and Streckeisen, 1991; Philpotts and Jay, 2009; Bissell, 2021). By  
126 contrast, in the mantle, we adopt two major oxides ( $Al_2O_3$  and FeO) as independent variables and compute the other  
127 CFMAS oxides (CaO, FeO, MgO,  $Al_2O_3$  and SiO<sub>2</sub>) from statistical correlations based on global mantle xenoliths and  
128 peridotite massifs databases (e.g., Afonso et al., 2013a,b; Fullea et al., 2021).

Deleted: Al2O3

Deleted: Al2O3

Deleted: databases

Deleted:

## 130 2.1 The geotherm.

131 In general, temperature increases with depth ( $z$ ) within the Earth. Heat transport inside the Earth is mainly a 3D problem  
132 in which the mantle is in convection at a high Rayleigh number ( $Ra > 10^7$ ; e.g., Ricard, 2007), bringing heat from the  
133 Core-Mantle Boundary, where the  $D''$  layer acts as the lower hot thermal boundary of the convection, up to the base of  
134 the thermal lithosphere, the Lithosphere-Asthenosphere Boundary (LAB). The LAB (usually defined by the 1250–1330  
135 °C isotherm; e.g., Grose and Afonso, 2019; Ball et al., 2021; Audhkhazi and Singh, 2022) represents the base of the  
136 portion of the upper mantle where viscosity is high enough ( $>10^{23}$  Pa s, e.g., Nakada, 1996) to prevent mantle convection,  
137 leaving conduction as the dominant heat transport process (e.g., Turcotte et al., 2007). The lithospheric geotherm controls  
138 the surface heat flow, which is an output of TCSEIS-1D.

Deleted: D''

Deleted: -

139 Here we are interested in a parametrization that reflects the temperature domain division between the lithosphere and the  
140 sublithospheric (upper and lower) mantle, ensuring energy budget consistency across the two domains and being flexible  
141 enough to model transient and steady-state thermal situations. The geotherm in TCSEIS-1D follows a 1D thermal  
142 parametrization, where the temperature varies only with depth ( $z$ ):

$$144 \rho(z)Cp(z) \frac{dT}{dt} = \frac{\partial}{\partial z} (k(z, T) \frac{\partial T}{\partial z}) + Hr(z) \quad (\text{Eq. 1})$$

145 where  $\rho(z)$  is the density,  $Cp(z)$  is the heat capacity,  $k(z, T)$  is the thermal conductivity, and  $Hr(z)$  is the radiogenic heat  
146 production as a function of depth (e.g., Gerya, 2007).

Deleted:

147 We solve Eq. 1 on an equispaced 1-km vertical grid using the Finite Differences technique with the following initial and  
148 boundary conditions:

- 149 - The temperature at the surface of the Earth is constant (and defined by the user).
- 150 - The temperature at the CMB is constant (and defined by the user).
- 151 - The LAB depth and temperature (e.g., 200 km and 1573 K) are defined by the user and are set as an inner boundary  
152 condition to the solution of Eq.1. This point is fixed in the solution (unless a collocated thermal anomaly is input by  
153 the user) and, therefore, it divides the temperature field into two domains: from the surface to the LAB (conductive  
154 geotherm, typically 5-25 K/km), and from the LAB to the CMB (convective geotherm, typically 0.25-0.6 K/km).
- 155 - The asthenospheric (or sublithospheric mantle, depth  $>$  LAB depth), the transitional mantle (or transition zone, i.e.,  
156 from 410 km to 660 km depth), and the lower mantle (depth  $>$  660 km) geotherms are defined by two initial  
157 temperature gradients provided by the user (by default, 0.45 K/km in the asthenosphere and transition zone, and 0.25  
158 K/km in the lower mantle). Therefore, below the lithosphere, a pseudo-convective geotherm is calculated by solving  
159 Eq. 1 for the initial conditions from the thermal gradients. In this way, we parametrize a continuous temperature

Deleted: pseudo-convective geotherm is calculated, solving Eq. 1 ...

169 gradient in the thermal buffer immediately below the lithosphere where both conduction and convective processes are  
170 expected.

171 - The time variable in Eq. 1 is, in general, taken large enough to reach thermal steady-state conditions. Transient thermal  
172 scenarios in the lithosphere can be modeled by adding the appropriate time input.

173 - Vertical variations in radiogenic heat production, thermal conductivity, and heat capacity are considered in the  
174 temperature modeling within TCSEIS-1D. The thermal conductivity of mantle rocks is computed according to the  
175 equation and parameters proposed by Hofmeister (1999) as a function of temperature, pressure, and predominant  
176 mineral type. In this work, we assume one representative mineral chosen from the pyrolite compositional model (e.g.,  
177 Ringwood, 1982; Irifune and Isshiki, 1998; Irifune et al., 2010; Hirose, 2006) for each mantle section in order to  
178 compute thermal conductivity: olivine (lithosphere and asthenosphere), ringwoodite (upper transition zone, from ~410  
179 km to ~550 km), wadsleyite (lower transition zone, from ~550 km to ~660 km), and bridgmanite (lower mantle; e.g.,  
180 Hamblin and Christiansen, 2004; Lin et al., 2013). The code also offers the possibility of adding thermal anomalies  
181 with respect to the conductive (lithosphere) and pseudo-convective geotherm (asthenosphere, transition zone, and  
182 lower mantle) computed as described above by setting a depth range and a temperature anomaly.

183  
184 Eq. 1 can model the geotherm in a variety of tectonic and geodynamic settings, for example: (a) continental and mature  
185 oceanic lithosphere in thermal steady state; (b) Mid-Oceanic Ridges and young oceanic lithosphere in transient thermal  
186 state; and (c) close to the adiabatic geothermal gradient below the lithosphere with the typical steep increase in  
187 temperature observed in the vicinity of the CMB.

188  
189 Note that we do not intend to solve a full geodynamic problem in the sublithospheric mantle (i.e., incorporating mantle  
190 flow and dynamic topography); instead, we aim for a flexible 1D parameterization able to describe variations in the  
191 geothermal gradient or temperature anomalies with respect to the reference geothermal gradients (e.g., plumes or slabs;  
192 see Section 4.2 for an example) as imaged by seismic data.

## 193 2.2 Compositional model space

194 To simplify the existing plethora of mineral aggregates (rocks), we have split the model compositional space ( $\mathcal{C}$ ) into  
195 three major categories: sedimentary rocks, igneous rocks, and mantle rocks. Out of these, only igneous rocks are further  
196 separated into three compositional subcategories: felsic, mafic, and ultramafic rocks (after standard geologic  
197 classification, e.g., Streckeisen, 1974). In this section, we describe how each rock type is parametrized and how the  
198 relevant geophysical parameters are computed from the  $\mathcal{JPC}$  triad. Metamorphic rocks have been left out of our model  
199 parametrization as their mineralogy tends to be complex, as well as some physical features that require complex numerical  
200 representation (e.g., distinctive and pronounced planes of weakness). Furthermore, their classification is usually based on  
201 texture and not composition, which makes it difficult to relate to our proposed parametrization. Therefore, we favor the  
202 use of their protoliths, which are much simpler to describe in terms of their mineral composition and properties. For  
203 example, a marble, composed of recrystallized carbonatic minerals, can be represented as a 0% porosity carbonate. This  
204 is a novel scheme as no rigorous thermochemical/lithological parametrization has been presented in previous tools  
205 designed for integrated modelling of the lithosphere (e.g., Afonso et al., 2008, 2013a,b; Fullea et al., 2009, 2021).

### 206 2.2.1 Sedimentary Rocks

207  
208 In TCSEIS-1D the sedimentary compositional space ( $\mathcal{C}$ ) is discretized following the simplest ternary diagram  
209 provided by Bissell (2021). Based on it, each corner of the ternary diagram stands for:

Deleted:

Deleted: ti

Deleted:

- 214 -  $\alpha$ -Quartz (Qz).  
215 - Carbonates: represented in our model by pure calcite ( $\text{CaCO}_3$ ) as it is much more common than dolomite  
216 ( $\text{CaMg}(\text{CO}_3)_2$ )  
217 - Clay Minerals ( $[\text{Al}, \text{Fe}]_2\text{O}_5$ ): representing a *mélange à parts égales* (from here onwards, mape) of three commonly  
218 occurring clay minerals: Montmorillonite + Kaolinite + Illite.

Deleted: à parts égales

219 We use the code MinVel (Hacker et al., 2004; Abers et al., 2016; Sowers et al., 2019), an extensive database of physical  
220 properties of minerals from laboratory measurements (Haker et al., 2004), to estimate  $V_p$ ,  $V_s$ , and  $\rho$  for all the  
221 compositional space ( $\mathcal{C}$ ), defined by the possible combinations of the minerals (3 values that add up to 100%, e.g., 60 %  
222 quartz + 20% carbonates + 20 % clays) every 10%, for different temperatures (between 200 and 1000 K every 100 K)  
223 and pressures (between 0 and 0.6 GPa every 0.025 GPa). This sampling yields three multidimensional grids (one for each  
224 property) in which rock properties are stored for a range of  $\mathcal{JPC}$  values. These are linearly interpolated and saved into  
225 easy-to-call Julia functions. In this way, we can estimate  $V_p$ ,  $V_s$  and  $\rho$  for a fully consolidated sedimentary unit from any  
226 given  $\mathcal{JPC}$  values (compositions are limited to triads consisting of multiples of 10 to guarantee numerical precision and  
227 computational speed). Fig. 2 presents several examples of the geophysical properties in ternary diagrams. Notice that  
228 carbonatic rocks tend to show larger velocity and density values than other lithologies, regardless of temperature, pressure  
229 conditions, or porosity, and clays show the largest variations.

Formatted: English (US)

### 231 2.2.2 Crustal Igneous Rocks

232 For crustal igneous rocks, we use a similar approach to that presented for sedimentary rocks in the previous section,  
233 including the use of mape where required and linear interpolation. In this case, three compositional subspaces are  
234 considered, one for each igneous rock subcategory: felsic, mafic and ultramafic rocks (as defined by Streckeisen, 1974;  
235 Le Bas and Streckeisen, 1991; Philpotts and Jay, 2009). We treat each subcategory as follows:

- 236 - Felsic rocks are defined in a ternary space outlined by the QAP diagram (quartz, K- feldspars, and plagioclase). We  
237 discard the standard QAFP classification (quartz, K- feldspars, feldspathoids, and plagioclase) in favor of a 3-mineral  
238 space as feldspathoids (F) resemble feldspars (K), and rocks with high concentrations of F are comparatively much  
239 less common. Hence, felsic rocks are defined by the ternary of:  $\alpha$ -quartz or  $\beta$ -quartz (as we account for the reversible  
240 change at 573 °C, which drastically impacts the determination of  $V_p$ ,  $V_s$ , and  $\rho$ ; Abers and Hacker, 2016); K- feldspars  
241 (a mape of Orthoclase + Sanidine); and Plagioclase (a mape of High Albite + Low Albite + Anorthite).  
242 - Mafic rocks are considered aggregates of: anorthosite (mape of Anorthite+High Albite+Low Albite), clinopyroxene  
243 (mape of Diopside+Hedenbergite) and orthopyroxene (mape of Enstatite+Ferrosilite).  
244 - Ultramafic rocks are defined as a combination of olivine (mape of Forsterite+Fayalite), clinopyroxene (mape of  
245 Diopside+Hedenbergite) and orthopyroxene (mape of Enstatite+Ferrosilite).

Deleted: feldspars

Deleted: feldspars

Deleted: feldspathoids

Deleted: feldspars

Deleted: ortopyroxene

246  
247 As with sedimentary rocks, we sample each compositional space with MinVel (Hacker et al., 2004; Abers et al., 2016;  
248 Sowers et al., 2019) at variations in composition every 10% for different crustal temperatures (between 0 and 1600 K  
249 every 100 K) and pressures (between 0 and 4 GPa every 0.05 GPa) and then save all results into Julia functions. In order  
250 to show the variations of the  $V_p$ ,  $V_s$ , and  $\rho$  values in a ternary diagram, Fig. 2 presents several examples.

Formatted: English (US)

Formatted: English (US)

252 Typical igneous rocks have very low primary porosity (e.g., 0.05%–0.90% for granite and 0.6–1.3 for basalts, Wieczysty,  
253 1982) when compared to sediments (e.g., a typical sandstone has a porosity ranging from 10% to 40%) and are usually  
254 found at high  $\mathcal{P}$  in the crust. Furthermore, even though crustal rocks are well known to have secondary porosity (e.g. high

261 density faulting), there is no simple way to account for it in  $V_p$ ,  $V_s$  or  $\rho$ . Therefore, we choose not to apply any porosity  
262 corrections for igneous rocks in TCSEIS-1D.

Deleted: ,

263  
264

### 265 2.2.3 Porosity

266 Crustal rocks are not perfect aggregates of minerals, and their behavior is not completely elastic in some cases. Rocks (in  
267 our case igneous and sedimentary) are generally porous, including secondary porosity and fractures, and hence we correct  
268 their geophysical properties by the percentage of porosity ( $\varphi$ ). Velocities ( $V_x$ ) are corrected in accordance with Raymer's  
269 equations (Raymer et al., 1980), while density ( $\rho$ ) is corrected following Athy's law (Athy, 1930):

Deleted: s

270  
271

$$V_{rock} = (1 - \varphi/100)^2 V_{solid} + (\varphi/100) V_{liquid} \text{ (Eq. 2)}$$

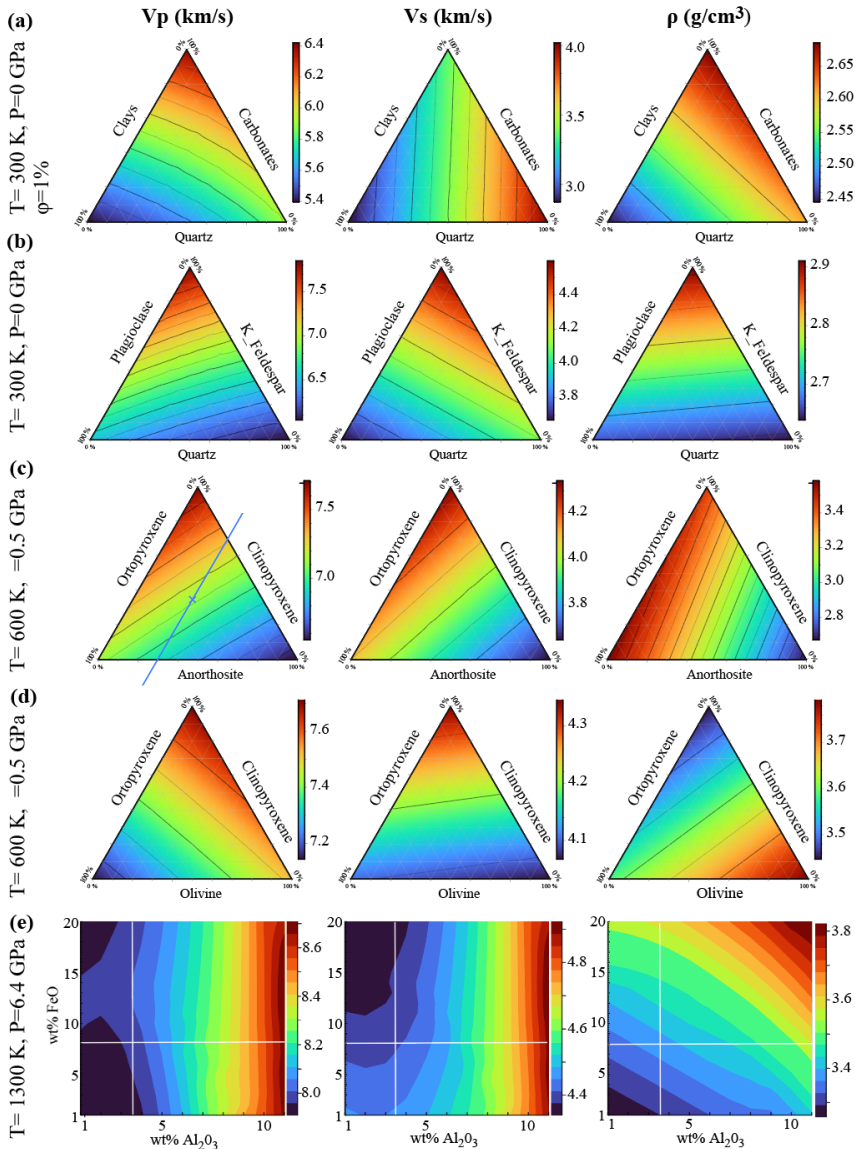
272  
273

$$\rho_{rock} = (\varphi/100 - 1) \rho_{solid} \text{ (Eq. 3)}$$

274 Where  $X_{rock}$  refers to the corrected property,  $X_{solid}$  to the property of the fully consolidated rock and  $X_{liquid}$  to the property  
275 of the fluid inside the porous space. The user must input  $X_{liquid}$  of the fluid inside the porous space, if not the corrections  
276 are applied by default as if the rocks were filled with air.

Deleted: scape

277



281  
282

283 Figure 2: Examples of compressional wavespeed ( $V_p$ ), shear wavespeed ( $V_s$ ) and density ( $\rho$ ) variations for: (a) **sedimentary**,  
 284 (b) igneous felsic, (c) igneous mafic, (d) igneous ultramafic and (e) mantle rocks as a function of temperature ( $T$ ), pressure ( $P$ ),  
 285 composition and porosity (for sedimentary rocks). All color scales are similar for ease of comparison. In sedimentary rocks (a)  
 286 **carbonates** have the higher  $V_p$  and  $\rho$ . For felsic rocks, with higher percentage of quartz,  $V_p$  and  $\rho$  becomes higher, while  $V_s$   
 287 becomes higher with the increase of plagioclase. Also, lower values of all three properties are associated with higher percentage  
 288 of **K-feldspars**. For mafic rocks, all properties increase with the percentage of **anorthosite** and **decrease** with the percentage of  
 289 **clinopyroxene**. Unlike felsic or mafic rocks, in ultramafics, each mineral dominates the decrease of a different property. On (e)  
 290 the cross marks the average mantle composition.

Deleted: sedimentray

Deleted: carbonatics

Deleted:

Deleted: decrease

### 295 2.2.3 Mantle Rocks

296 Compared to the crust, the Earth's mantle petrology is less complex and can be adequately represented by the modal  
297 distribution of the main mineral phases (olivine, pyroxenes, and Al-bearing phases) under the consideration of  
298 thermodynamic equilibrium ( $T > 500$  °C). In this work we determine stable mantle mineral assemblages using a Gibbs  
299 free energy minimization scheme (Connolly, 2005, 2009). Therefore, the mantle's physical properties relevant to our  
300 work ( $V_p$ ,  $V_s$  and  $\rho$ ) are computed on these assumptions based on the  $\mathcal{JPC}$  values. A standard characterization of mantle  
301 composition is based on the main major oxides in the CFMAS system (CaO–FeO–MgO–Al<sub>2</sub>O<sub>3</sub>–SiO<sub>2</sub>; e.g. Irifune, 1990;  
302 Irifune and Tsuchiya, 2015). To simplify the parametrization of  $\mathcal{C}$ , here we adopt the discretization of Fullea et al. (2021)  
303 where the wt% amounts Al<sub>2</sub>O<sub>3</sub> and FeO oxides in the mantle layers are free variables, and CaO–MgO amounts are  
304 statistically correlated to Al<sub>2</sub>O<sub>3</sub> based on global petrological databases as described in Afonso et al. (2013a). Similarly to  
305 Mg# (= MgO/[MgO + FeO]), Al<sub>2</sub>O<sub>3</sub> has been shown to be a strong compositional indicator and, therefore, an overall  
306 proxy for mantle fertility. Mantle fertility refers to the relative enrichment of the mantle in basaltic, melt-producing  
307 components, such as basaltic components and thus to its potential to generate partial melting. In particular a fertile mantle  
308 should be rich in Al<sub>2</sub>O<sub>3</sub>, CaO, FeO, meaning more content of clinopyroxene and garnet while a depleted mantle has  
309 residue after melt extraction like harzburgitic and low Al<sub>2</sub>O<sub>3</sub>. In contrast, neither FeO nor SiO<sub>2</sub> are correlated in general  
310 with either CaO or Al<sub>2</sub>O<sub>3</sub> (Afonso et al. 2013a). For the petrological calculations we use Perple\_X (Connolly, 2005, 2009)  
311 and for the lower mantle the databases by Xu et al. (2008) and Stixrude & Litgow-Bertelloni (2021). We sample the wide  
312 range of  $\mathcal{T}$  (from 100 to 4500 K) and  $\mathcal{P}$  (from 0 to 145 GPa) found in the mantle. As for the self-consistent thermodynamic  
313 database, in the upper mantle we use the Xu et al. (2008), whereas in the transition zone and lower mantle we consider  
314 Stixrude & Litgow-Bertelloni (2021).  $\mathcal{C}$  values are limited to the ranges of (1-11) wt% for Al<sub>2</sub>O<sub>3</sub> and (1-20) wt% for FeO.  
315 This range of compositions should be more than enough to model almost every scenario in the entire mantle as values of  
316 Al<sub>2</sub>O<sub>3</sub> are expected to range from 1.0 wt% to 6.0 wt% and FeO is generally considered to be around 8.0 wt% (e.g.,  
317 McDonough and Sun, 1995). In some special cases larger ranges might be needed, e.g., Large Low Shear Velocity  
318 Provinces in the lowermost mantle (e.g., Vilella et al., 2021). In Fig. 2 we show the relevant mantle properties for several  
319  $\mathcal{JP}$  conditions.

320 In TCSEIS-1D, there are four major mantle layers defined by their wt% amounts of Al<sub>2</sub>O<sub>3</sub> and FeO:

- 321 1) The *lithospheric mantle* extends from the Moho down to the Lithosphere-Asthenosphere Boundary, or LAB (an input  
322 depth and temperature are expected from the user as explained in Section 2.2). The thickness of this layer is user-defined  
323 and does not change unless thermal anomalies are incorporated into the model.
- 324 2) The *asthenospheric (or sublithospheric) mantle* extends from the LAB down to a pressure of ~14 GPa, representing  
325 the average value for the transition from olivine to wadsleyite mineral phases.
- 326 3) The *transition zone mantle* extends from a pressure of ~14 GPa to a value of ~24 GPa. The later value is the average  
327 pressure for the transition from ringwoodite and majorite to perovskite and ferropericlae, the boundary between the upper  
328 and the lower mantle. Note that the transition zone includes an inner phase transition from wadsleyite to ringwoodite at  
329 around 520 km depth (Rigden et al., 1991; Tian et al., 2020).
- 330 4) The *lower mantle* extends from a pressure of ~24 GPa down to the CMB (a user input).

331 While the boundaries between the first two layers (i.e., LAB depth) and the bottom of the model (i.e., CMB) are input  
332 parameters, in the case of the top and bottom of the mantle transition zone, the depth depends on different mineral phase  
333 transitions that cannot be predicted beforehand without performing a thermodynamic calculation based on the actual  $\mathcal{JPC}$   
334 conditions. Therefore, our approach here is to initially define those mantle layer boundaries based on standard reference  
335 pressure values (~14 GPa and ~24 GPa), and subsequently relocate them automatically to the depth at which the relevant

Deleted:

Deleted: such as and thus to its potential to generate partial.

Formatted: Font: Times New Roman, 10 pt, Font color: Accent 3

Formatted: Subscript

Deleted: b

Formatted: English (US)

Deleted:

Deleted: ,

Deleted: ese

Formatted: English (US)

342 phase transitions occur. Therefore, from a compositional point of view, the depth of the base of layer 2 and 3 is effectively  
343 defined by a thermodynamic equilibrium calculation. In virtue of the thermodynamic parametrization, the velocity and  
344 density jumps related to phase transitions usually associated with the 410 km, 520 km, and 660 km discontinuities will  
345 arise in the model even if the composition is uniform across all four mantle layers. For example, all these discontinuities  
346 still appear in the model for a constant whole mantle composition (e.g., primitive mantle composition with 3.6 wt%  $\text{Al}_2\text{O}_3$   
347 and 8.0 wt% FeO from McDonough and Sun, 1995). Finally, the user can also specify anomalous regions (compositional  
348 anomalies) within any of the four compositional layers by setting a depth range and a chemical anomaly value (e.g., -0.5  
349 wt%  $\text{Al}_2\text{O}_3$  and +0.2 wt% FeO).

350

### 351 2.2.3.1 Seismic attenuation in the mantle

352 To account for anelasticity, we follow the strategy of Dannberg et al. (2017) and extrapolate the relationships for olivine  
353 at upper mantle conditions derived by Jackson and Faul (2010) to the whole mantle. Notice that this is clearly a  
354 simplification of the mineralogy at the mantle scale and thus its behavior in seismic attenuation terms, but Dannberg et  
355 al. (2017) proved that it yields a useful first-order approximation as the results are not very dissimilar to, for example, the  
356 values reported in the PREM model. Here we adopt the parametrization by Dannberg et al. (2017) as described in  
357 Appendix B.

358

359 Most of the attenuation parameters are different for each major mantle mineral phase. In TCSEIS-1D, we use different  
360 attenuation parameters for the most abundant mineral phases at each depth depending on their respective stability fields:  
361 the upper mantle (olivine), the upper and lower transition zones (wadsleyite and ringwoodite), and the lower mantle  
362 (perovskite). Grain size ( $d$ ) has a large impact on the attenuation, as per our parametrization described in Appendix B. In  
363 the code, the user can choose between three grain size models with depth: (a) a constant value ( $d = 10$  mm), (b) the model  
364 by Schierjott et al. (2020), in which  $d$  increases with depth, and (c) the model by Dannberg et al. (2017), where  $d$  decreases  
365 with depth. In general terms, we find that the constant and Schierjott models fit best with the general trends of the global  
366 1D models (Fig. 3).

367

Formatted: Subscript

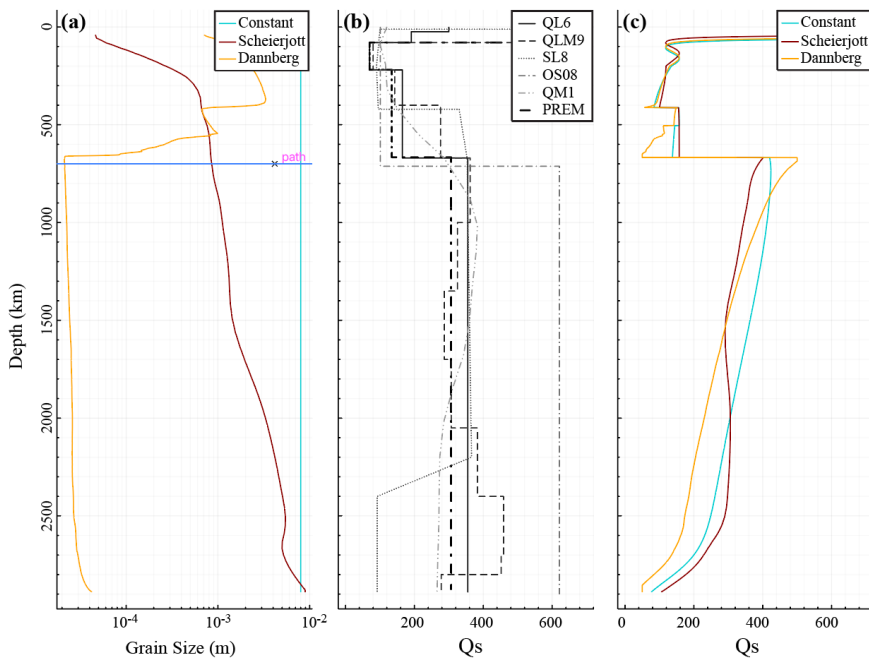
Formatted: Subscript

Deleted: 2O3

Deleted: Al2O3

Formatted: English (US)

Formatted: English (US)



370  
371

372 **Figure 3: (a) Grain size variation with depth for the 3 models included in the code: Constant (a constant value of  $10^{-2}$  m),**  
 373 **Schieerjott (the grain size variations estimated by Schierjott et al., 2020) and Dannberg (the grain size variations estimated by**  
 374 **Dannberg et al., 2017). (b) Several 1D radial models of  $Q_s$  for the whole mantle: SL8 (Anderson and Hart, 1978), QM1 (Widmer**  
 375 **et al., 1991), QL6 (Durek and Ekstrom, 1996), QLM9 (Lawrence and Wysession, 2006), QOS08 (Oki and Shearer, 2008), PREM**  
 376 **(Dziewonski and Anderson, 1981). (c)  $Q_s$  computed from the Burgers model of linear viscoelasticity (Jackson and Faul, 2010).**  
 377 **The Constant and Schierjott models produce the closest fit to the radial models.**

Deleted: r  
Deleted: R  
Deleted: of

#### 378 2.2.4 Melt

379 Accounting for melt in a 1D column requires the definition of consistent solidus and liquidus curves for the crust and the  
 380 whole mantle. In the crust, we consider the equations in Gerya (2019) characterizing the solidus and liquidus temperatures  
 381 for sediments and igneous rocks. In the mantle, water content and, to a lesser extent, composition control the solidus  
 382 values reported in the literature (e.g., Schmidt and Poli, 1998; Hirschmann, 2000; Katz et al., 2003; Sarafian et al., 2016;  
 383 Fu et al., 2018). In TCSEIS-1D, we allow the user to define the solidus curve for the upper mantle (i.e., from the Moho  
 384 to a pressure of ~ 10 GPa or depth of ~300 km) from two sources:

- 385 - The solidus presented by Andraut et al. (2018), which corresponds to a nominally dry mantle (between 1 and 90 wt  
 386 ppm),
- 387 - The second-degree polynomial by Katz et al. (2003), defined only up to 7 GPa, which corresponds to a nominally  
 388 anhydrous mantle with 40–80 wt ppm of water.

389  
 390 From 10 GPa to 30 GPa, we use the logarithmic anhydrous solidus curve by Herzberg et al. (2000), and from 30 GPa to  
 391 120 GPa, the solidus curve by Fu et al. (2018) with ~ 400 wt ppm water can be extrapolated to the CMB conditions,  
 392 according to the authors.

396 For the mantle liquidus, we use (a) a fourth-degree polynomial fitted to the liquidus curve by Litasov and Ohtani (2002),  
 397 valid from 0 GPa (surface) to ~30 GPa (roughly 800 km depth), and (b) a second-degree polynomial fitting the liquidus  
 398 curve by Fu et al. (2018) from 30 GPa to the CMB. With this parametrization, the solidus and liquidus curves have large  
 399 jumps at the crust-mantle boundary and around 800 km, therefore we have chosen to smooth them with a loess (Fig. 11).  
 400 The volumetric melt fraction (Melt) is usually defined, for a constant pressure, as a linearly varying temperature-  
 401 dependent function (e.g., Gerya and Yuen, 2003b; Burg and Gerya, 2005; Gerya, 2019; Fullea et al., 2021):

$$402 \quad \text{Melt} = 0\% \text{ from } T \leq T_{\text{solidus}} \text{ (Eq. 4)}$$

$$405 \quad \text{Melt} = \frac{(T - T_{\text{solidus}})}{(T_{\text{liquidus}} - T_{\text{solidus}})} 100 \text{ from } T_{\text{solidus}} < T < T_{\text{liquidus}} \text{ (Eq. 5)}$$

$$407 \quad \text{Melt} = 100\% \text{ at } T \geq T_{\text{liquidus}} \text{ (Eq. 6)}$$

409 where  $T_{\text{solidus}}$  and  $T_{\text{liquidus}}$  are the wet solidus and dry liquidus temperatures defined by the curves described previously.  
 410 Once  $\text{Melt}(z)$  has been computed for each model node, the associated seismic parameters ( $V_p$ ,  $V_s$ ,  $Q_s$ ) are corrected  
 411 following the experimental study by Chantel et al. (2016):

$$412 \quad V_p = 0.07\text{Melt}^2 - 0.5566\text{Melt} + 7.9235 \text{ (Eq. 7)}$$

$$414 \quad V_s = 0.065\text{Melt}^2 - 0.5565\text{Melt} + 4.4211 \text{ (Eq. 8)}$$

$$416 \quad 100/Q_s = 2.4063\ln(\text{Melt}) + 5.9284 \text{ (Eq. 9)}$$

418 Mantle density is corrected (becoming the effective density,  $\rho_{\text{eff}}$ ) by the equation postulated by Gerya (2019):

$$419 \quad \rho_{\text{eff}} = \rho_{\text{solid}}(1 - \text{Melt} + \text{Melt} \frac{\rho_{\text{molten}}}{\rho_{\text{solid}}}) \text{ (Eq. 110)}$$

420 where  $\rho_{\text{solid}}$  and  $\rho_{\text{liquid}}$  are the standard densities of the solid and molten rock, respectively, and  $\rho_{\text{solid}}$  is the density of the  
 421 solid rock at the given  $T, P$  conditions computed as described in section 2.1 and 2.3. The values for  $\rho_{\text{solid}}$  and  $\rho_{\text{liquid}}$  are  
 422 taken from the compilation of values by Gerya (2019) and could be changed by the user inside the code if required. Figure  
 423 4 shows the used curves.

Formatted: English (US)

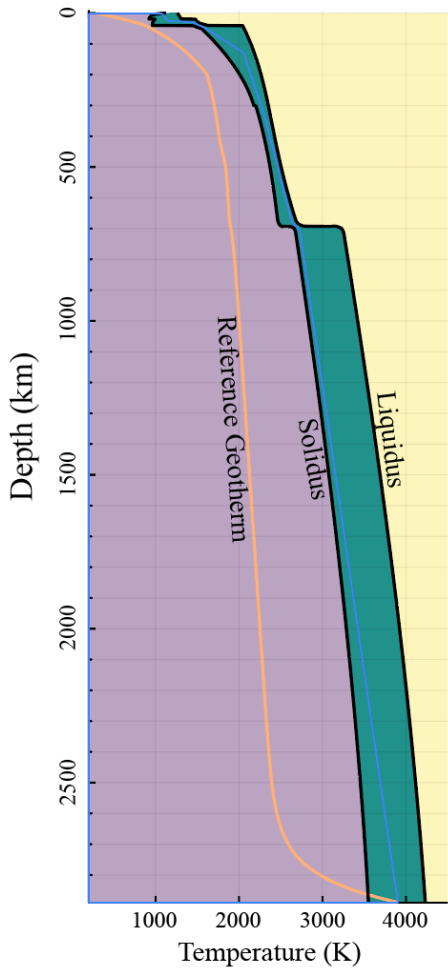


Figure 4: Solidus and liquidus curves from the entire crust and mantle. Solidus by: Gerya (2019), Katz et al.(2003), Herzberg et al (2000) and Fu et al.(2018). Liquidus by: Gerya (2019), Litasov and Ohtani (2002) and Fu et al.(2018). See text for details.

Deleted: ,  
 Deleted: ,  
 Deleted: ,

435  
 436  
 437  
 438  
 439  
 440  
 441  
 442  
 443  
 444  
 445

449 **2.4 Surface Wave Dispersion Forward Modeling**

450 TCSEIS-1D computes surface wave dispersion curves in two ways: from a native function SWD.jl (developed as part of  
451 TCSEIS-1D) or by calling Mineos.jl, a Julia wrapper around the code Mineos developed to compute normal modes of the  
452 Earth (Master et al., 2011, <https://geodynamics.org/cig>). In general terms, SWD.jl is faster than Mineos.jl, although the  
453 former gives an approximated solution in contrast to the exact solution from the latter. Both codes run on CPU and the  
454 computation time for a dispersion curve with 20 samples, for PREM model is in the order of 0.17 s for SWD.jl and 0.26  
455 s for Mineos.jl on an Apple MacBook Air with 8 GB of RAM and M1 chip. Also, the approximations built in SWD.jl  
456 yield some high errors (>1%) in cases of very strong attenuation ( $Q_s < 70$ ) and high-order overtone calculation.

457  
458 SWD.jl is mostly based on the formulation described by Haney and Tsai (2015, 2017, 2019). These authors utilize (for  
459 both Rayleigh and Love waves) a finite element approach based on the thin-layer method (Lysmer, 1970; Kausel, 2005).  
460 The scheme behind SWD.jl and the corrections necessary to approximate the results from Mineos.jl are detailed in  
461 Appendix A. To validate both approaches, in Fig. 5, we present a comparison between surface wave dispersion curves  
462 computed by SWD.jl (the main TCSEIS-1D dispersion engine), Mineos.jl (Masters et al., 2011) and the exact solution.  
463 Each code uses a different approach for the computation: SWD.jl uses a finite element solution, whereas Mineos uses the  
464 traditional normal-mode summation. Discrepancies in the results from all three codes are small in terms of phase velocity  
465 ( $dc < 0.045\%$ ) and group velocity ( $dU < 0.2\%$ ) and might arise from the difference in the computations and/or  
466 parameterization of the model for each code. For example, at  $T = 50$  s, considering the PREM velocity model as input,  
467 the fundamental mode Rayleigh wave phase velocity differences comparing the output of the three codes are  $< 0.002\%$ .  
468 Notice that errors increase with time because of the spherical approximation. The user can always extract the standard  
469 seismic velocities and density geophysical model from the TCSEIS-1D output to perform customized seismic modeling  
470 a posteriori with other tools. We recommend using Mineos.jl for modeling data with long periods ( $T > 70$  s, shorter  
471 periods are properly represented by SWD.jl), higher overtones (overtones 1 and 2 are well computed by SWD.jl but higher  
472 overtones are not well represented by the FEM formulation), and for studying regions with strong attenuation (as SWD.jl  
473 uses an approximation to attenuation, see Appendix B for details). Note that the original Mineos code has a limitation of  
474 300 velocity layers, making it only appropriate for  $T > 30$  s. On the other hand, SWD.jl is recommended for shorter  
475 periods ( $T < 70$  s; mainly crust and upper mantle studies) where complex models can be proposed or when computational  
476 time is relevant.

477

Deleted: run

Deleted: in

Deleted: i

Deleted: and

Formatted: English (US)

Formatted: English (US)

Deleted: in

Deleted: d

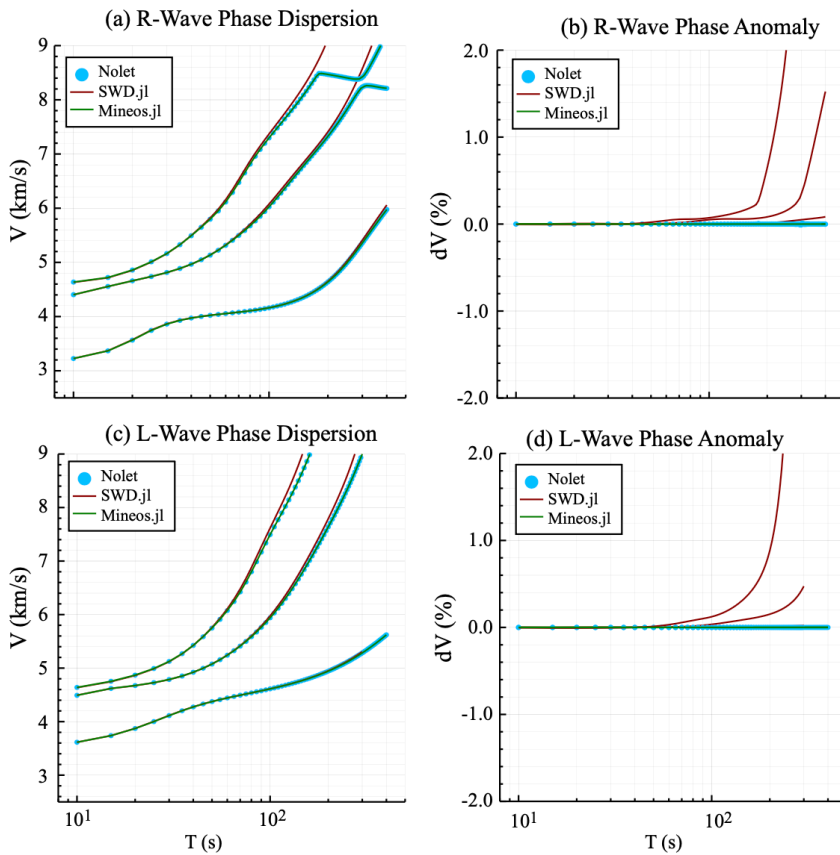


Figure 5: Comparison between surface wave dispersion curves computed by SWD.jl (red, the main TCSEIS-1D dispersion engine), Mineos (green, Masters et al., 2011) and the exact solution (blue circles marked as Nolet).

### 2.5 Receiver Functions Forward Modeling

In order to give the user a basic handling of receiver function data during the modeling stages, we have incorporated a simple module (i.e., the computation is made without accounting for the effect of anisotropy or attenuation) to compute synthetic receiver functions from the input geophysical model. Receiver functions are computed using a transfer function between the stress and displacement known as the propagator matrix approach (Thomson, 1950; Haskell, 1953; Kennett, 1983). For all the receiver functions, P-to-S, S-to-P, and SKS-to-P, the sequence is similar. For each source (with a depth and epicentral distance taken from the IASP91 tables; Kennett et al., 1991), the synthetic radial and vertical components (R and Z) are computed for a given 1D model and then rotated into the direction of polarization of the incident P-wave (L) and its perpendicular (Q) in the R-Z plane (e.g., Vinnik, 1977; Kind et al., 1995). In general, we compute the surface response in the Fourier domain for a plane impingement waveform. The transmitted impulse is assumed to arrive at the

Formatted: English (US)

Deleted: I

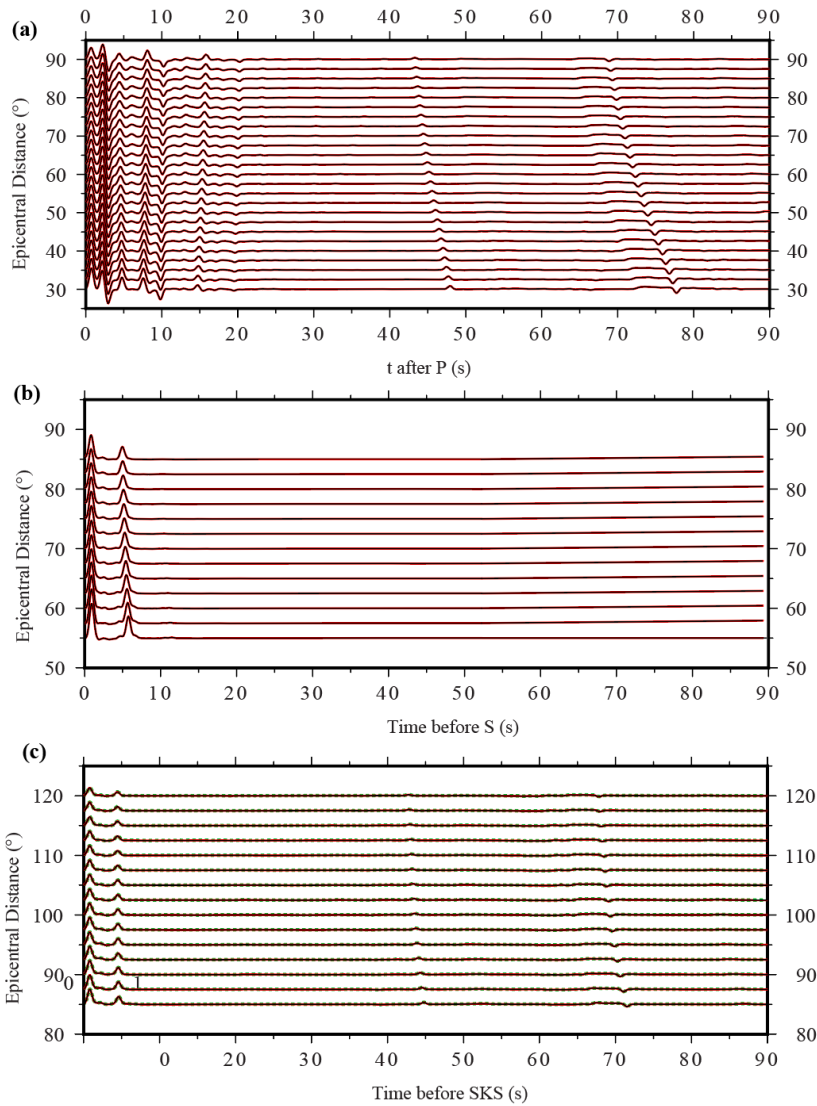
500 surface at  $t = 0$  s. Then, we calculate the time domain displacements at the surface for each direction. The computation  
501 includes all multiples, transformations, and reflections produced by an arbitrary structure with homogeneous layers  
502 (Svenningsen and Jacobsen, 2007). Finally, the Z (or L) component records are deconvolved from the R (or Q)  
503 components, and a Gaussian low-pass filter is applied to the resulting seismogram. For the S wave incidence, the resultant  
504 seismograms are subject to time and sign reversals, following the convention for S receiver functions (e.g., Yuan et al.,  
505 2006). This process is repeated  $n$  times (as many RFs are input by the user) for a list of events (epicentral distances and  
506 depths). The resulting  $n$  receiver functions are stacked via move-out correction considering the IASP91 model and a  
507 reference velocity of 6.4 km/s (e.g., Rondenay, 2009). The final stacked receiver functions are compared with the  
508 observed waveforms to measure misfits. Fig. 6 shows a comparison between the results of the RF computations in  
509 TCSEIS-1D and those from other codes in order to validate the results.

510 For these comparisons (and by default in the code), RF are normalized, as amplitude values may vary with instruments  
511 and processing. No other corrections are applied to the final stack, and the post-processing (if required) is left to the end  
512 user. Furthermore, attenuation and anisotropy effects are not accounted for, the code automatically outputs a geophysical  
513 model ( $z$ ,  $V_p$ ,  $V_s$ ,  $\rho$ ,  $Q_s$ ,  $\gamma$ ) that can be used for forward computation and individual RF for post-processing using other  
514 modelling tools. It is important to keep in mind that real RF are highly dependent on the quality of the data and the steps  
515 used by the interpreter. In general, there are several ways to approach the deconvolution of the horizontal and vertical  
516 components of the seismogram that may differ from the scheme presented here (e.g., Pesce, 2010). Here, we use the now-  
517 classic implementation of the frequency-domain water-level algorithm (e.g., Langston, 1979; Rondenay, 2009). Hence,  
518 when modeling real RF with TCSEIS-1D, care must be taken to consider the aforementioned points for consistency,  
519 especially regarding anisotropy and attenuation.

520  
521  
522  
523  
524  
525  
526  
527  
528  
529  
530  
531  
532  
533

Deleted: I

Formatted: English (US)



535  
536  
537  
538  
539  
540  
541  
542  
543

Figure 6: Comparison between the synthetic Receiver Functions (RF) computed by the code and those computed with other codes. (a) P-to-S RF, (b) S-to-P RF and (c) SKS-to-P RF. RF in red correspond to our code, those in black were computed with the Matlab codes by Bo Holm Jacobsen (2008; Svenningsen and Jacobsen, 2007), and in green those computed in IRFFM2 V1.2 (Tkalčić et al., 2012, only P-to-S available). Differences are small (error < 0.1%). For this example, the Gaussian parameter  $\sigma = 2.5$  (roughly between 0.4 and 1 Hz).

Formatted: English (US)  
Deleted: o  
Deleted: Difference  
Deleted: For this example the gaussian parameter

547 **3. Testing TCSEIS-1D: Sensitivity analysis**

548 To illustrate the capabilities of TCSEIS-1D, we present three simple examples that demonstrate the sensitivity of Rayleigh  
549 wave phase velocity curves and P-to-S receiver functions to compositional and temperature variations with respect to a  
550 reference model (Figures 14–16). The reference model in our examples is characterized by:

- 551
- 552 i. A 40-km-thick crust with a 2-km shale sedimentary layer (Qz(%)=30, Carbo(%)=10, Clays(%)=60, Porosity(%)=5), a  
553 20 km thick monzodioritic (felsic) upper crust (Qz(%)=10, K-feldspar(%)=90, Plagioclase(%)=0), and a 20-km thick  
554 orthopyroxene-gabbroic (mafic) lower crust (Anorthosite(%)=20, Clinopyroxene(%)=60, Orthopyroxene(%)=20).
  - 555 ii. A 200-km-thick lithosphere with a LAB temperature of 1300 °C.
  - 556
  - 557 iii. A uniform whole mantle composition:  $Al_2O_3=3.6$  wt% and  $FeO=8.0$  wt% (e.g., McDonough and Sun, 1995) with  
558 constant grain size (10 mm).
  - 559 iv. Isotropic model (i.e., no radial anisotropy)
- 560

561 **3.1 Example 1: Average Mantle Composition**

562 In this first example (Fig. 7), we change the composition of the entire mantle. The values for the two independent oxides  
563 in our parametrization ( $Al_2O_3 = 3.6$  wt% and  $FeO = 8.0$  wt%) correspond to the primitive mantle composition from  
564 McDonough and Sun (1995). Here, we explore the effect of changing the value of  $Al_2O_3$  to 2.0 wt% and to 5.0 wt% (for  
565 a constant value of  $FeO$  wt%). Then, the effect of changing the values of  $FeO$  to 6.0% and 10.0% (for a constant value of  
566  $Al_2O_3$  wt%). From this simple test, we can draw a few important conclusions:

567 - The amount of  $Al_2O_3$  dominates the velocity gradients in the upper mantle, with velocity variations being proportional  
568 to  $Al_2O_3$  content. However,  $Al_2O_3$  has a limited effect on the lower mantle.

569 - The amount of  $FeO$  dictates the velocity gradients in the lower mantle while having a minor effect in the upper mantle.

570 In general terms, velocity gradients are inversely proportional to the wt% of  $FeO$  in the lower mantle. Interestingly  $FeO$   
571 has a dramatic effect on the gradient at the top of the D'' layer, changing its depth by ~100 km within our test.

572 - The sharpness and depth of the transition zone boundaries is controlled by mantle composition. Both  $Al_2O_3$  and  $FeO$   
573 appear to have a dramatic effect on the 410 km discontinuity (olivine->wadsleyite) sharpness. By contrast, the 560 km  
574 discontinuity (wadsleyite->ringwoodite) and the 660 km discontinuity (ringwoodite+majorite->perovskite+ferropericlasite) are mostly affected by  $FeO$  and  $Al_2O_3$  respectively.

575 We note that within the chemical parametrization in TCSEIS-1D, the amount of  $CaO$  and  $MgO$  oxides is dependent on  
576 the amount of  $Al_2O_3$  based on statistical correlations from global petrological databases (Afonso et al., 2013a). By  
577 contrast, the amount of  $FeO$  is an independent variable.

579

Deleted: .  
Formatted: English (US)

Deleted: K-feldspar

Formatted: English (US)

Deleted: Al2O3

Formatted: English (US)

Formatted: English (US)

Formatted: English (US)

Formatted: English (US)

Formatted: Subscript

Formatted: Subscript

Formatted: Subscript

Formatted: Subscript

Formatted: Subscript

Formatted: Subscript

Deleted: Al2O3

Deleted: Al2O3

Deleted: Al2O3

Formatted: Subscript

Formatted: Subscript

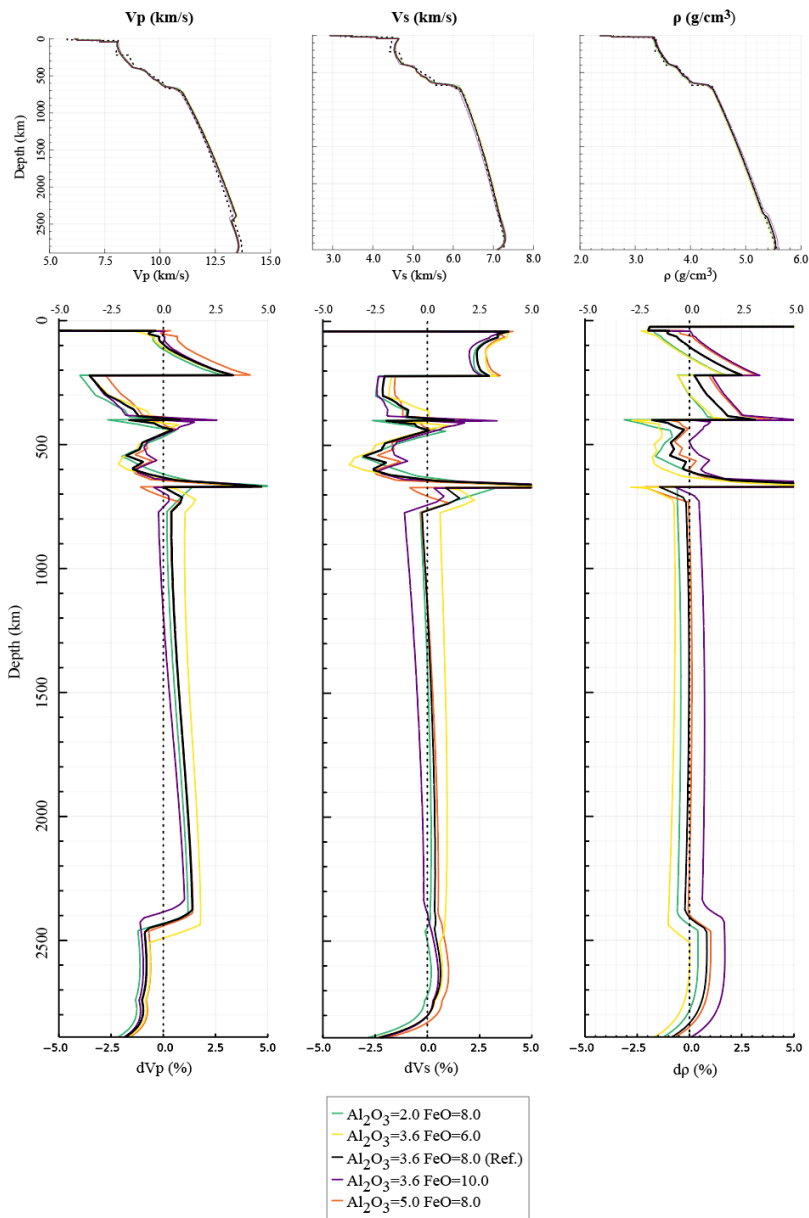
Formatted: Subscript

Formatted: Subscript

Deleted: ;

Formatted: Subscript

Formatted: Subscript



588  
589  
590  
591  
592  
593  
594

Figure 7: Example 1. Comparison between the results of a constant composition mantle in TCSEIS-1D (solid lines) and the PREM model (dashed). Here we have tested several compositions to show how large  $V_p$ ,  $V_s$  and  $\rho$  anomalies can arise from extreme values of  $Al_2O_3$  and FeO. Top panels show the comparison in absolute  $V_p$ ,  $V_s$  and  $\rho$  values, while the bottom panel shows anomalies with respect to PREM. In the bottom panel, crustal anomalies have been deleted from the presentation as they are too large since PREM has a poorly estimated crust.

- Formatted: English (US)
- Formatted: English (US)
- Deleted: Rho
- Deleted: Rho
- Formatted: Subscript
- Formatted: Subscript
- Deleted: as PREM has a poorly estimated crust

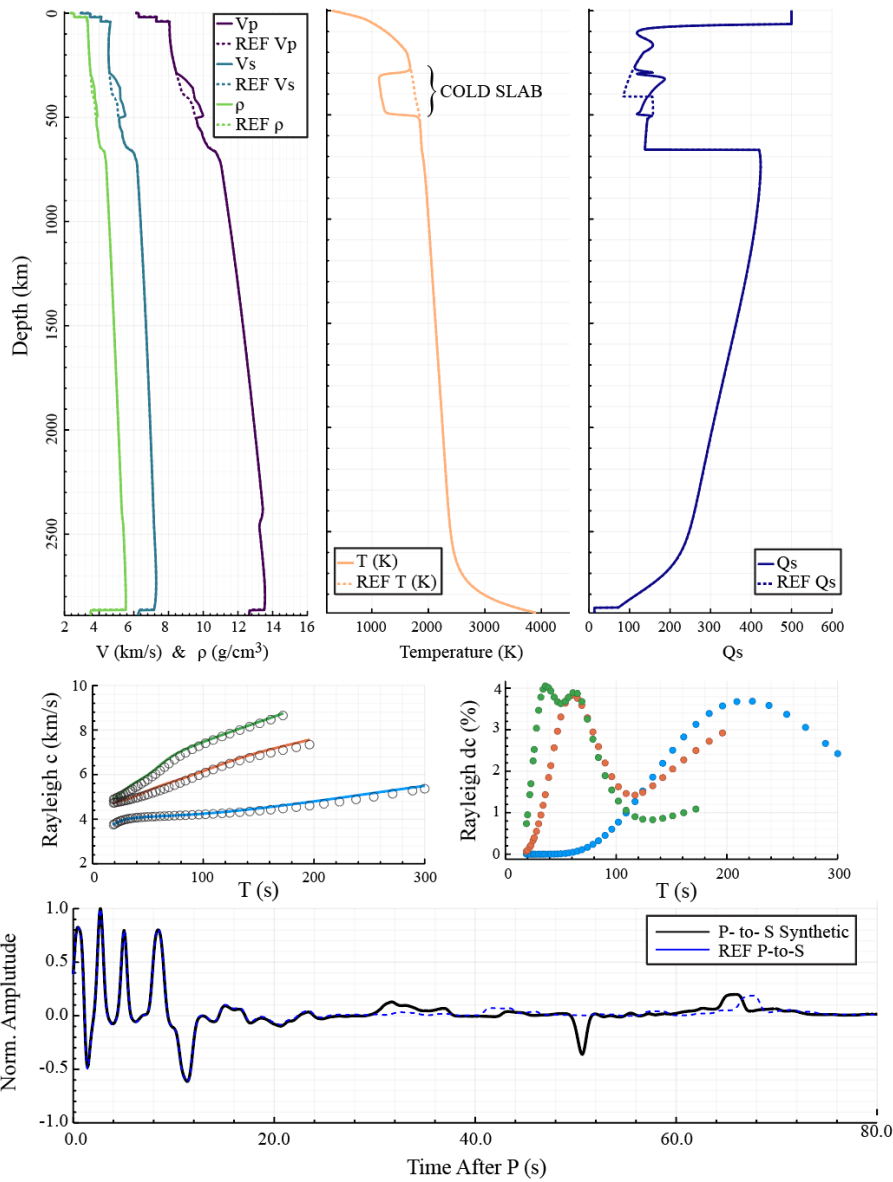
598 **3.2 Example 2: Cold horizontally stagnating slab**

599 In the second example (Fig. 8), we implement a thermal and compositional anomaly with respect to the reference model  
600 representing a 1D section of a cold horizontally stagnating slab (a subducted slab that changes direction in the transition  
601 mantle; e.g., Fukao et al., 2009). The anomaly is defined from 300 km to 500 km depth (Fig. 14) and is characterized by:  
602 (a) a -600 K thermal anomaly with respect to the ambient mantle; and (b) a chemical anomaly of  $Al_2O_3 = -0.25$  wt% with  
603 respect to our reference model. The mantle in the “slab” region shows higher values for velocities, density, and  $Q_s$  than  
604 the reference model. These positive anomalies are easily recognized in the Rayleigh wave dispersion curves: for the long  
605 periods in the fundamental mode and, in general, for the higher dispersion modes, the phase velocity anomalies are >  
606 +3%. The P-to-S receiver function is only modified for periods > 20 s (arrival of late phases) due to the upward shift of  
607 the 410 km discontinuity caused by the “slab” anomaly.  
608

Formatted: English (US)

Deleted: Al2O3

Deleted: "



611  
 612 Figure 8: Example 2 showing the effect of a cold slab-like feature plunging into the transition zone. On the top: the left panel  
 613 show the  $V_p$ ,  $V_s$  and  $\rho$  profiles with depth (solid lines are the computed parameters and dashed ones are the PREM values), in  
 614 the center we show the temperature profile with (T) and without (Ref T), and on the right the attenuation profile with ( $Q_s$ )  
 615 and without (Qs Ref). On the center of the figure we present: on the left the dispersion curves of the model with (solid  
 616 lines) and without (circles) the slab for the fundamental mode (blue) and the 1st (orange) and second (green) overtones.  
 617 Anomalies between both are presented in the right panel. At the bottom P-to-S RF with (black) and without (blue) are shown.  
 618 Notice that, except for the first panel, Ref is the reference model without anomalies (see text for details).

619

Deleted: s  
 Deleted: Rho  
 Deleted: re

623 **3.3 Example 3: Hot ponding plume head**

624 In the third example (Fig. 9), we implement a thermal and compositional anomaly with respect to the reference model  
625 representing a 1D section of a hot horizontally flowing or ponding plume head (wide horizontal zones that extend from  
626 the vertical plume conduct at discontinuities; e.g., Dongmo Wamba et al., 2023). The “plume” is the anomaly, which is  
627 defined from 600 km to 900 km depth (Fig. 15) and is characterized by: (a) a +600 K thermal anomaly with respect to the  
628 ambient mantle; and (b) a chemical anomaly of  $Al_2O_3 = +0.25$  wt% and  $FeO = +0.5$  wt%. The “plume” anomaly shows  
629 lower values for the velocities, density, and  $Q_s$  than the reference model. In this case, the anomalous region is divided  
630 into two sections: the upper part (600 km–700 km depth) with extremely low anomalies (caused by melting atop the  
631 plume), and the lower part (depth > 700 km) where the decrease in the physical parameters is less pronounced. The  
632 temperature and composition anomalies strongly affect synthetic Rayleigh wave dispersion curves. For the long periods  
633 in the fundamental mode, and in general for the higher dispersion modes, the phase velocity anomalies are < -5%. The P-  
634 to-S receiver function is modified for periods > 40 s as all the lower part of the transition zone is affected by the anomaly,  
635 which also generates sharp impedance contrasts. It is worth noting that the effect of the anomaly in this example is so  
636 significant that the crustal phases recorded in the receiver functions are slightly affected as well.  
637

Formatted: English (US)

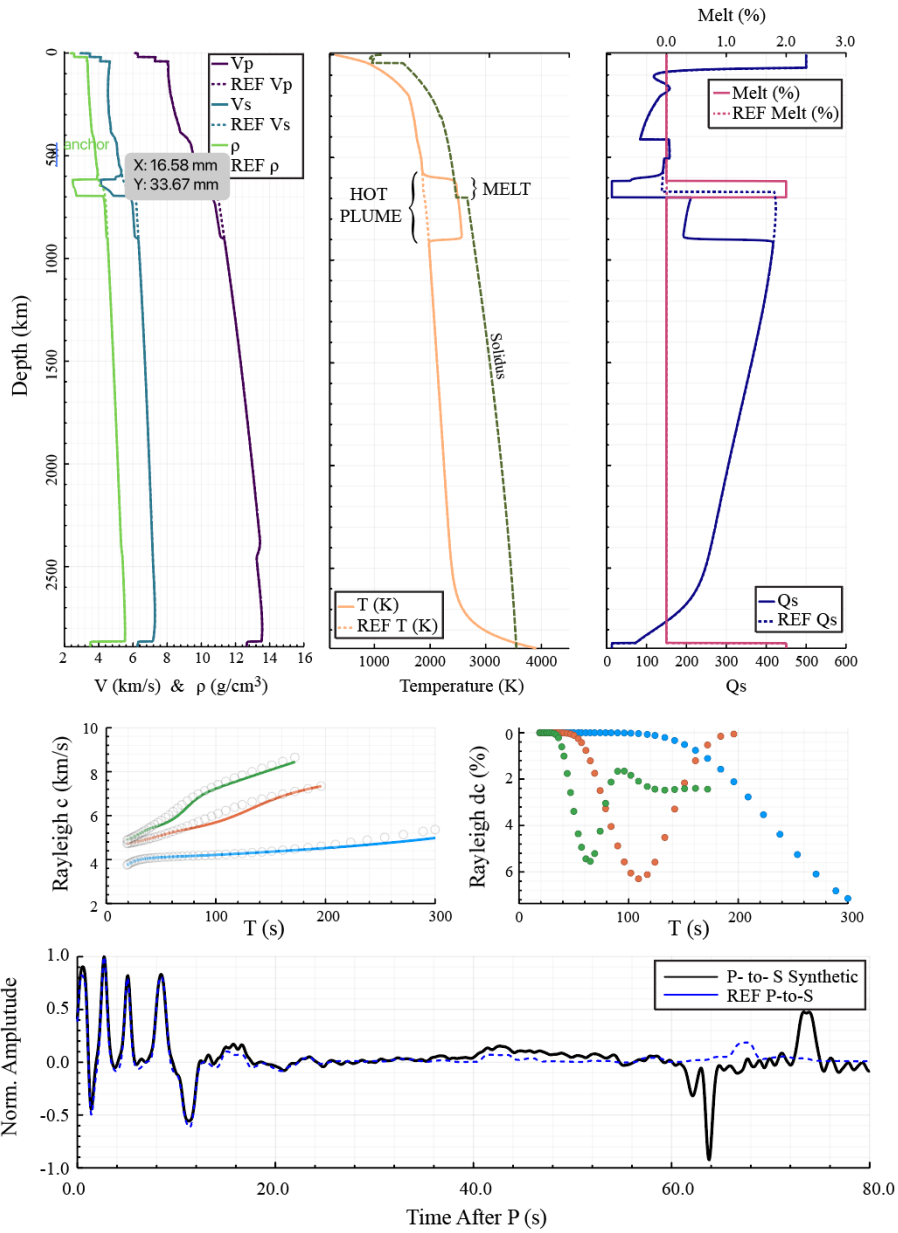
Deleted:

Deleted: 2

Deleted: 3

Formatted: Subscript

Formatted: Subscript



641  
642  
643  
644  
645  
646

Figure 9: Example 3 showing the effect of a hot plume-like feature entering the transition zone from below. Panels are in the same configuration as in Fig. 8, but in this case we add the melt curve to the top right plot.

Deleted: 2

Deleted: are

Formatted: English (US)

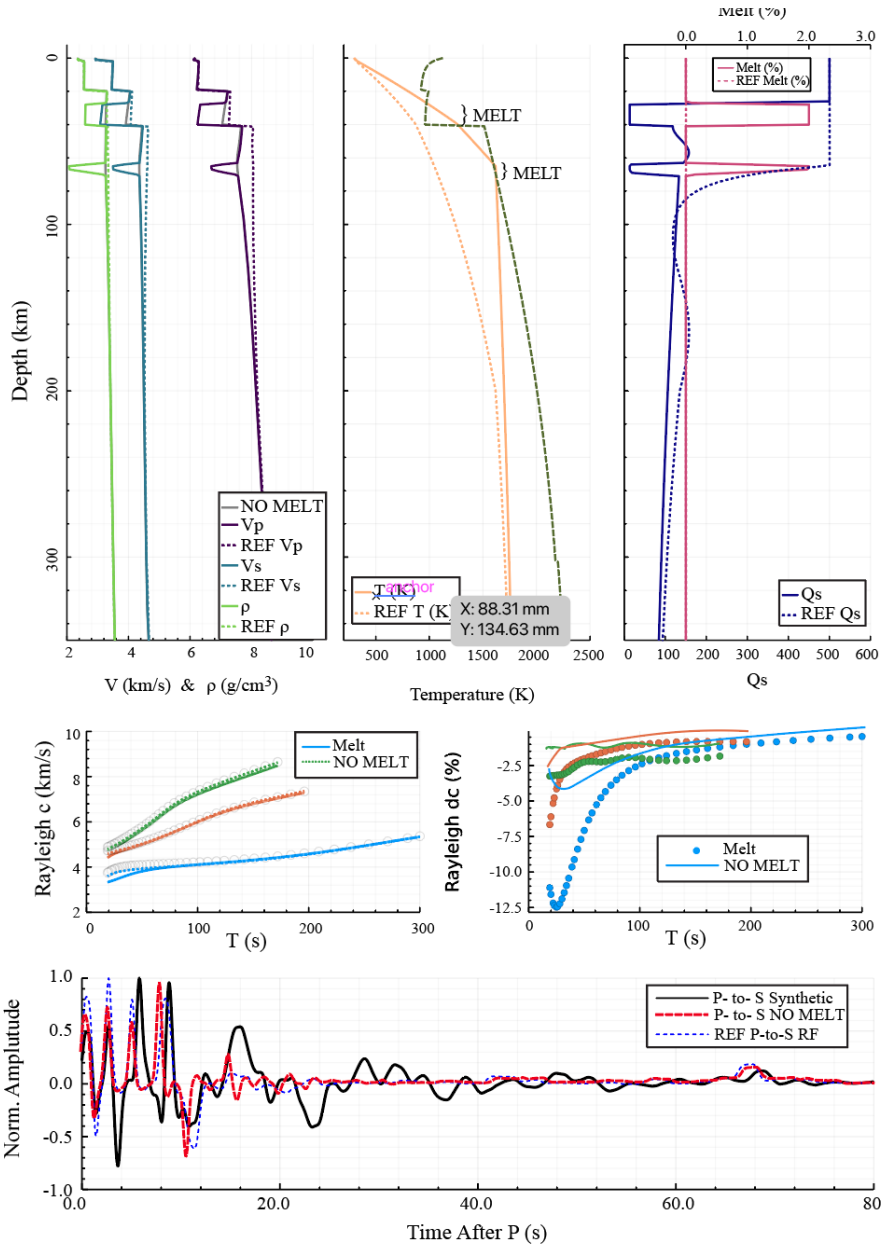
649 **3.3 Example 4: Thin Lithosphere**

650 In the final example, we leave most parameters from the reference model constant and change the base of the lithosphere  
651 from 200 km in the reference model to 60 km (Fig. 16). This change has a drastic effect on the model as two melt regions  
652 appear, one near the LAB and the other at the base of the crust, causing two low-velocity, density, and Qs regions at 35  
653 km and 70 km depth, respectively. The effect of the lithospheric thinning is strong in the predicted surface wave dispersion  
654 curves, in particular for the fundamental mode, where large negative anomalies are apparent, and less so for the overtones.  
655 The waveform of the P-to-S receiver function drastically changes due to the negative impedance present within the crust  
656 and upper mantle in our example model. The effect is much less dramatic but still present if the melt modeling option is  
657 turned off.

Deleted:

Deleted:

Deleted: s



661  
662  
663  
664  
665

Fig. 10 : Example 4 showing the effect of a thin lithosphere under an average continental crust. Panels are the same as in Fig. 8. Here we show two outputs: with melt (MELT, same as in previous examples) and without melt (NO MELT, dotted lines).

Deleted: 3

Formatted: English (US)

667 **4. Remarks, conclusions and further work**

668 Receiver functions and surface wave dispersion data analysis has led to remarkable results revealing the Earth's internal  
669 structure in terms of compressional and shear waves velocity anomalies ( $\delta V_p$ ,  $\delta V_s$ ). Yet, the interpretation of these  
670 anomalies in terms of crustal and mantle composition is a challenging modeling task. The usage of these data under  
671 geophysical-petrological schemes has proven to yield important results in terms of the thermal and petrological structure  
672 of the Earth's mantle (e.g. Munch et al., 2018; Bissig et al., 2021; Afonso et al., 2022; Fullea et al., 2021; Munch et al.,  
673 2021; Lebedev et al., 2024 ). Yet, the usage of this type of method is not common.

674 In order to build a bridge to go from classical seismological approaches to the thermal-petrological realm, we present  
675 TCSEIS-1D, a new, open-source, cross-platform, easy-to-use, and accurate code to model the crust and whole mantle  
676 using surface wave dispersion curves (including group and phase velocity of Rayleigh and Love waves for the  
677 fundamental mode, as well as several overtones) and three widely used receiver functions (P-to-S, S-to-P, and SKS-to-P)  
678 directly in terms of rock composition and the in-situ temperature and pressure conditions. We achieved this by creating  
679 an interface between the modeling of seismic data and mineral/phase equilibria calculations that allow for the calculation  
680 of elastic properties (i.e.,  $V_p$ ,  $V_s$ , and density) as a function of temperature, pressure, and composition. Moreover,  
681 TCSEIS-1D can be used as a simple geophysical model (i.e., seismic velocities and density) generator based on input  
682 thermochemical conditions that can be coupled to third-party seismic codes to perform forward calculations, offering as  
683 well a variety of tools intended to interpret geophysical data and models in petrological (e.g., property maps in the  $TPC$   
684 space; Fig. 1) and geodynamical terms (e.g. different thermal scenarios, Figs. 14-16).

685 TCSEIS-1D can be used to simultaneously fit different real seismological and other geophysical data sets within a trial-  
686 and-error approach or to carry out synthetic modeling (e.g., sensitivity analysis), making it a useful tool for a wide range  
687 of geoscientists. Future work includes developing an inversion scheme of seismic data for the thermochemical structure  
688 of the crust and mantle based on TCSEIS-1D.

689  
690

691  
692  
693  
694  
695  
696  
697  
698  
699  
700  
701  
702  
703  
704  
705  
706

Deleted: l

Deleted: ve

Deleted: s

710

711 **Appendix A: TCSEIS-1D Surface Wave Dispersion native package: SWD.jl**

712 SWD.jl is mostly based on the formulation described by Haney and Tsai (2015, 2017, 2019). These authors utilize (for  
 713 both Rayleigh and Love waves) a finite element approach based on the thin-layer method (Lysmer, 1970; Kausel, 2005).  
 714 In contrast to the popular Thomson-Haskell recursion formula (e.g., Takeuchi and Saito, 1972; Saito, 1988), Haney and  
 715 Tsai employed several thin layers leading to a generalized eigenvalue/eigenvector problem that must be solved for every  
 716 sampled frequency ( $1/T_{\text{Observed}}$ , Hz). Their method is both accurate and fast and allows for the consideration of a water  
 717 layer on top of the model column. However, as originally proposed, the method is hampered by two shortcomings: (1) it  
 718 assumes the Earth is isotropic, elastic and flat, and (2) it requires the specification of a relatively dense Finite Elements  
 719 (FEM) mesh. We address each one of these as follows:

720

721 (a) We decouple the computation of Rayleigh and Love waves based on the vertically and horizontally polarized  
 722  $V_s(\mathcal{TPC})$  components,  $V_{SV}$  and  $V_{SH}$ , respectively defined as:

$$723 \quad V_{SV} = (1 - \frac{1}{3}\chi)V_S \text{ (Eq. A.1)}$$

$$724 \quad V_{SH} = (\frac{2}{3}\chi + 1)V_S \text{ (Eq. A.2)}$$

725 Where  $\chi$  is the average seismic radial anisotropy for each layer (user input). Rayleigh and Love dispersion curves  
 726 are computed as a function of  $V_{SV}$  and  $V_{SH}$  respectively.

727

728 We include anelastic effects as stated by Karato, (1993), Minster and Anderson (1981), Afonso et al. (2005), Fullea et al.  
 729 (2021), using the expressions:

$$730 \quad V_{Pa} = V_P (1 - \frac{2}{9} \cot(\frac{\pi\alpha}{2}) Q_s^{-1}) \text{ (Eq. A.3)}$$

$$731 \quad V_{Sa} = V_S (1 - \frac{1}{2} \cot(\frac{\pi\alpha}{2}) Q_s^{-1}) \text{ (Eq. A.4)}$$

732 Where,  $V_{Pa}$  and  $V_{Sa}$  are the anelastic P and S velocities, and  $V_p$  and  $V_s$  are the anharmonic velocities computed from  
 733  $\mathcal{TPC}$  values. Further details on estimating  $Q_s$  are presented in section 2.6.

734 (b) We consider the Earth's sphericity correcting the values of  $V_p$ ,  $V_s$  and  $\rho$  for the Earth-flattening approximation  
 735 before computing the dispersion curves. Here, we follow Herrmann (2013) for Rayleigh waves, and the equations  
 736 by Schwab and Knopoff (1972) for Love waves. The depth from the surface in the equivalent flat Earth model,  
 737  $z$ , is given by:

$$738 \quad z = a \ln \frac{a}{r} \text{ (Eq. A.5)}$$

739 Where  $r$  is the radial distance from the center of the Earth, and  $a$  is the Earth's radius. Hence, if we consider a  
 740 spherical layer bounded by  $r_i$  and  $r_{i-1}$  radii, with  $r_{i-1} > r_i$ , then the thickness,  $h$ , of the corresponding  $i^{\text{th}}$  flat layer is  
 741 given by:

$$742 \quad (h_i)_f = a \ln \left( \frac{a}{r_i} \right) - a \ln \left( \frac{a}{r_{i-1}} \right) \text{ (Eq. A.6)}$$

743 The mean  $V_p$ ,  $V_s$  and  $\rho$  in the transformed flat layer model,  $(V_p)_f$ ,  $(V_s)_f$ ,  $(\rho)_f$  and are given by

$$744 \quad (V_p)_f = (V_p)_s \frac{2a}{r_i + r_{i-1}} \text{ (Eq. A.7)}$$

$$745 \quad (V_s)_f = (V_s)_s \frac{2a}{r_i + r_{i-1}} \text{ (Eq. A.8)}$$

$$746 \quad (\rho)_f = (\rho)_s \left( \frac{2a}{r_i + r_{i-1}} \right)^{SE} \text{ (Eq. A.9)}$$

Deleted: i

Deleted: via

749 Where  $(V_p)_s$ ,  $(V_s)_s$ ,  $(\rho)_s$  are the mean  $V_p$ ,  $V_s$  and  $\rho$  in the spherical model, and  $SE$  is a parameter that takes a different  
750 value for Love ( $SE=-5$ , Schwab and Knopoff, 1972) and Rayleigh (we find a better fit with an exponent value of  $SE=-$   
751  $2.278$  instead of  $SE=-2.275$  as originally reported in Herrmann (2013)).  
752

753 (c) Finally, we optimize the FEM mesh for the forward computation (e.g., Xia et al., 1999, Ma and Clayton, 2016,  
754 Hanney and Tsai, 2015, 2017, 2019). Generally, the required mesh must have adequate sampling above the  
755 sensitivity depth of each period, without oversampling the model below it unnecessarily. As a rule of thumb,  
756 more than five 5 layers (6 nodes) are required in the sensitivity depths of each frequency with their thicknesses  
757 increasing exponentially from the surface to the bottom of the model (e.g., Hanney and Tsai, 2017). In TCSEIS-  
758 1D, the user has two possibilities: (i) using a precomputed mesh (the Golden Mesh) created with smaller layers  
759 than those required to compute the dispersion at any period between 1 s and 500 s, and slightly oversampling  
760 the base of the model; or (ii) using a new mesh based on the lowest period of the input data and a low threshold  
761 of Rayleigh wave phase velocity set to 1 km/s (see Hanney and Tsai, 2017, Appendix D for more details). Our  
762 mesh samples all the space, and the thickness of each layer coincides with the sensitivity of both Rayleigh waves  
763 and Love waves (depending on the period). Our FEM grids for surface waves are designed to compute dispersion  
764 curves in the period range from 5 s to 500 s.  
765  
766  
767  
768  
769  
770  
771  
772  
773  
774  
775  
776  
777  
778  
779  
780  
781  
782  
783  
784  
785  
786  
787  
788  
789

790 **Appendix B: seismic attenuation model**

791

792 Dannberg et al. (2017) pose that the response of a continuum that behaves according to Burgers model of linear  
 793 viscoelasticity with creep function in response to a sinusoidally time-varying stress (e.g., a dispersive wave) is given by  
 794 the dynamic compliance  $J^*(\omega)$  (the Laplace transform of its creep function). This function takes the form:

795 
$$J^*(\omega) = J_1(\omega) + iJ_2(\omega) \text{ (Eq. B1)}$$

796 
$$J_1 = J_u \left\{ 1 + \frac{\alpha \Delta_B}{\tau_H^\alpha - \tau_L^\alpha} \int_{\tau_L}^{\tau_H} \frac{\tau^{\alpha-1}}{1+\omega^2 \tau^2} d\tau + \frac{\Delta_P}{\sigma \sqrt{2\pi}} \int_0^\infty \frac{1}{\tau(1+\omega^2 \tau^2)} \exp\left(-\frac{\ln(\frac{\tau}{\tau_P})^2}{2\sigma^2}\right) d\tau \right\} \text{ (Eq. B2)}$$

797 
$$J_2 = J_u \left\{ \frac{\omega \alpha \Delta_B}{\tau_H^\alpha - \tau_L^\alpha} \int_{\tau_L}^{\tau_H} \frac{\tau^\alpha}{1+\omega^2 \tau^2} d\tau + \frac{\omega \Delta_P}{\sigma \sqrt{2\pi}} \int_0^\infty \frac{1}{1+\omega^2 \tau^2} \exp\left(-\frac{\ln(\frac{\tau}{\tau_P})^2}{2\sigma^2}\right) d\tau + \frac{1}{\omega \tau_M} \right\} \text{ (Eq. B3)}$$

798 Where  $\omega$  is the angular frequency,  $\omega = 2\pi/T$ ,  $\alpha$  is the anelastic frequency exponent,  $\Delta_B$  is the Burgers element strength  
 799 and  $\Delta_P$  and  $\sigma$  are the peak height and width, and  $J_u$  is the unrelaxed compliance (which is not computed for  $Q_s$   
 800 estimations).

801 All the timescales  $\tau_i$  control the temperature, pressure, and grain size sensitivity of the anelastic scaling relationships:

802

803 
$$\tau_i = \tau_{iR} \left(\frac{d}{d_R}\right)^{m_i} \exp \left[ \left(\frac{E^*}{R}\right) \left(\frac{1}{T} - \frac{1}{T_R}\right) + \left(\frac{V^*}{R}\right) \left(\frac{P}{T} - \frac{P_R}{T_R}\right) \right] \text{ (Eq. B4)}$$

804 where  $i = H, L, P, M$  are the upper, lower, peak and Maxwell viscous relaxation values respectively, and all  $m_i$  are grain  
 805 size exponents with  $j=H, L, P$  for anelastic relaxation ( $m_a$ ), and  $j=M$  for viscous relaxation ( $m_v$ ). Here,  $E^*$  and  $V^*$  are the  
 806 activation energy and volume for the anelastic model. We use the same values for each major mantle zone as reported in  
 807 the supplementary material of Dannberg et al. (2017). The temperature, pressure, and grain size sensitivity of the anelastic  
 808 relationships are introduced in terms of reference values  $T_R, P_R$  and  $d_R$ .

809 
$$Q_s = \frac{J_1(\omega)}{J_2(\omega)} \text{ (Eq. B5)}$$

810 and

811 
$$Q_p = \frac{9}{4} Q_s \text{ (Eq. B6)}$$

812 which implies an infinite quality factor for the bulk modulus (e.g., Karato, 1993; Minster and Anderson, 1981).

813

814

815

816

817

818

819

820

821

822

823

824

825

Formatted: English (US)

Deleted: implicates an infinite quality factor

827 **Acknowledgements**

828

829 MA was funded by Comunidad Autonoma de Madrid (Spain) through an “Atracción de Talento” senior fellowship (2018-  
830 T1/AMB/11493) to JF, who is also supported the Spanish Ministry of Science and Innovation (PID2020-114854GB-C22  
831 and CNS2022-135621).

832 **Data Availability Statement**

833 The full TCSEIS-ID v1.0 package is openly available for download at the project’s GitHub repository  
834 (<https://github.com/marianoarnaiz/TCSEIS>). The software requires a functional installation of the Julia Language  
835 (version 1.7 or higher) to run

836

837 **Author contribution statement:**

838 MA and JF co-designed the algorithms, and co-wrote the manuscript. MA wrote the code in Julia language. JF supervised  
839 the research project and tested the code.

840

841

842

843

844

845

846

847

848

849

850

851

852

853

854

855

856

857

858

859

860

861

862

863

864

865

866

867

868

869

870

- 871 **References**
- 872 Abers, G. A. and Hacker, B. R.: A MATLAB toolbox and Excel workbook for calculating the densities, seismic wave  
873 speeds, and major element composition of minerals and rocks at pressure and temperature, *Geochem. Geophys.*  
874 *Geosyst.*, 16, 616–624, <https://doi.org/10.1002/2015GC006091>, 2016.
- 875 Afonso, J. C., Ranalli, G., and Fernández, M.: Thermal expansivity and elastic properties of the lithospheric mantle:  
876 results from mineral physics of composites, *Phys. Earth Planet. Int.*, 149, 279–306,  
877 <https://doi.org/10.1016/j.pepi.2004.09.008>, 2005.
- 878 Aki, K., Christoffersson, A., and Husebye, E. S.: Determination of the 3-dimensional seismic structure of the  
879 lithosphere, *J. Geophys. Res.*, 82, 277–296, <https://doi.org/10.1029/JB082i002p00277>, 1977.
- 880 Andrault, D., Pesce, G., Manthilake, G., Monteux, J., Bolfan-Casanova, N., Chantel, J., Novella, D., Guignot, N., King,  
881 A., Itié, J.-P., and Hennet, L.: Deep and persistent melt layer in the Archaean mantle, *Nat. Geosci.*, 11, 139–143,  
882 <https://doi.org/10.1038/s41561-017-0053-9>, 2018.
- 883 Arnaiz-Rodríguez, M. S., Zhao, Y., Sánchez-Gamboa, A. K., and Audemard, F.: Crustal and upper-mantle structure of  
884 the Eastern Caribbean and Northern Venezuela from passive Rayleigh wave tomography, *Tectonophysics*, 804, 228711,  
885 <https://doi.org/10.1016/j.tecto.2020.228711>, 2020.
- 886 Athy, L. F.: Density, porosity and compaction of sedimentary rocks, *AAPG Bull.*, 14, 1–24,  
887 <https://doi.org/10.1306/3D9322C5-16B1-11D7-8645000102C1865D>, 1930.
- 888 Audkhkhasi, P. and Singh, S. C.: Discovery of distinct lithosphere-asthenosphere boundary and the Gutenberg  
889 discontinuity in the Atlantic Ocean, *Sci. Adv.*, 8, eabn5404, <https://doi.org/10.1126/sciadv.abn5404>, 2022.
- 890 Ball, P. W., White, N. J., MacLennan, J., et al.: Global influence of mantle temperature and plate thickness on intraplate  
891 volcanism, *Nat. Commun.*, 12, 2045, <https://doi.org/10.1038/s41467-021-22323-9>, 2021.
- 892 Bezanson, J., Edelman, A., Karpinski, S., and Shah, V. B.: Julia: A Fresh Approach to Numerical Computing, *SIAM*  
893 *Rev.*, 59, 65–98, <https://doi.org/10.1137/141000671>, 2017.
- 894 Bissell, H. J., Haaf, E. T., Crook, K. A. W., Beck, K. C., Schwab, F. L., and Folk, R. L.: Sedimentary rocks,  
895 *Encyclopædia Britannica*, <https://www.britannica.com/science/sedimentary-rock>, accessed 9 Dec 2021.
- 896 Bissig, F., Khan, A., Tauzin, B., Sossi, P. A., Münch, F. D., and Giardini, D.: Multifrequency inversion of Ps and Sp  
897 receiver functions: methodology and application to USArray data, *J. Geophys. Res. Solid Earth*, 126, e2020JB020350,  
898 <https://doi.org/10.1029/2020JB020350>, 2021.
- 899 Bosch, M.: Lithologic tomography: from plural geophysical data to lithology estimation, *J. Geophys. Res.*, 104, 749–  
900 766, <https://doi.org/10.1029/1998JB900035>, 1999.
- 901 Boujibar, A., Bolfan-Casanova, N., Andrault, D., Bouhifd, M. A., and Trcera, N.: Incorporation of Fe<sup>2+</sup> and Fe<sup>3+</sup> in  
902 bridgmanite during magma ocean crystallization, *Am. Mineral.*, 101, 1560–1570, <https://doi.org/10.2138/am-2016-5561>, 2016.
- 903

Formatted: English (US)

Formatted: Font: Bold, Text Outline

904 Brocher, T. M.: Empirical relations between elastic wavespeeds and density in the Earth's crust, *Bull. Seismol. Soc.*  
905 *Am.*, 95, 2081–2092, <https://doi.org/10.1785/0120040090>, 2005.

906 Calò, M., Bodin, T., and Romanowicz, B.: Layered structure in the upper mantle across North America from joint  
907 inversion of long and short period seismic data, *Earth Planet. Sci. Lett.*, 449, 164–175,  
908 <https://doi.org/10.1016/j.epsl.2016.05.054>, 2016.

909 Chen, X., Park, J., and Levin, V.: Anisotropic layering and seismic body waves: deformation gradients, initial  
910 S-polarizations, and converted-wave birefringence, *Pure Appl. Geophys.*, 178, 2001–2023,  
911 <https://doi.org/10.1007/s00024-021-02755-6>, 2021.

912 Connolly, J. A. D.: Computation of phase equilibria by linear programming: a tool for geodynamic modeling and its  
913 application to subduction zone decarbonation, *Earth Planet. Sci. Lett.*, 236, 524–541,  
914 <https://doi.org/10.1016/j.epsl.2005.03.039>, 2005.

915 Connolly, J. A. D.: The geodynamic equation of state: What and how, *Geochem. Geophys. Geosyst.*, 10, Q10014,  
916 <https://doi.org/10.1029/2009GC002540>, 2009.

917 Dinari, O., Yu, A., Freifeld, O., and Fisher, J.: Distributed MCMC inference in Dirichlet process mixture models using  
918 Julia, in *Proc. IEEE/ACM CCGrid*, 518–525, <https://doi.org/10.1109/CCGRID.2019.00066>, 2019.

919 Dongmo Wamba, M., Montagner, J.-P., and Romanowicz, B.: Imaging deep-mantle plumbing beneath La Réunion and  
920 Comores hot spots: vertical plume conduits and horizontal ponding zones, *Sci. Adv.*, 9, eade3723,  
921 <https://doi.org/10.1126/sciadv.ade3723>, 2023.

922 Faul, U. H. and Jackson, I.: The seismological signature of temperature and grain size variations in the upper mantle,  
923 *Earth Planet. Sci. Lett.*, 234, 119–134, <https://doi.org/10.1016/j.epsl.2005.02.030>, 2005.

924 Fullea, J., Afonso, J. C., Connolly, J. A. D., Fernández, M., García-Castellanos, D., and Zeyen, H.: LitMod3D: an  
925 interactive 3-D software to model the thermal, compositional, density, seismological, and rheological structure of the  
926 lithosphere and sublithospheric upper mantle, *Geochem. Geophys. Geosyst.*, 10, Q08019,  
927 <https://doi.org/10.1029/2009GC002391>, 2009.

928 Fullea, J., Lebedev, S., Martinec, Z., and Celli, N. L.: WINTERC-G: mapping the upper mantle thermochemical  
929 heterogeneity from coupled geophysical–petrological inversion of seismic waveforms, heat flow, surface elevation and  
930 gravity satellite data, *Geophys. J. Int.*, 226, 146–191, <https://doi.org/10.1093/gji/ggab094>, 2021.

931 Fukao, Y., Obayashi, M., and Nakakuki, T.: Stagnant slab: a review, *Annu. Rev. Earth Planet. Sci.*, 37, 19–46,  
932 <https://doi.org/10.1146/annurev.earth.36.031207.124224>, 2009.

933 Gao, K., Mei, G., Piccialli, F., Cuomo, S., Tu, J., and Huo, Z.: Julia language in machine learning: algorithms,  
934 applications, and open issues, *Comput. Sci. Rev.*, 37, 100254, <https://doi.org/10.1016/j.cosrev.2020.100254>, 2020.

935 Gerya, T.: *Introduction to Numerical Geodynamic Modelling*, Cambridge University Press, Cambridge, pp. 345,  
936 <https://doi.org/10.1017/CBO9780511809101>, 2009.

937 Grand, S. P.: Mantle shear-wave tomography and the fate of subducted slabs, *Philos. Trans. R. Soc. Lond. A*, 360,  
938 2475–2491, <https://doi.org/10.1098/rsta.2002.1023>, 2002.

939 Grose, C. J. and Afonso, J. C.: Chemical disequilibria, lithospheric thickness, and the source of ocean island basalts, *J.*  
940 *Petrol.*, 60, 755–790, <https://doi.org/10.1093/petrology/egz012>, 2019.

941 Hacker, B. R. and Abers, G. A.: Subduction Factory 3: an Excel worksheet and macro for calculating the densities,  
942 seismic wave speeds, and H<sub>2</sub>O contents of minerals and rocks at pressure and temperature, *Geochem. Geophys.*  
943 *Geosyst.*, 5, Q01005, <https://doi.org/10.1029/2003GC000649>, 2004.

944 Hamblin, W. K. and Christiansen, E. H.: *Earth's dynamic systems*, 10th edn., Prentice Hall, Upper Saddle River, NJ,  
945 790 pp., 2004.

946 Haney, M. M. and Tsai, V. C.: Nonperturbational surface-wave inversion: a Dix-type relation for surface waves,  
947 *Geophysics*, 80, EN167–EN177, <https://doi.org/10.1190/geo2014-0208.1>, 2015.

948 Haney, M. M. and Tsai, V. C.: Perturbational and nonperturbational inversion of Rayleigh-wave velocities, *Geophysics*,  
949 82, F15–F28, <https://doi.org/10.1190/GEO2016-0542.1>, 2017.

950 Haney, M. M. and Tsai, V. C.: Perturbational and nonperturbational inversion of Love-wave velocities, *Geophysics*, 85,  
951 F19–F26, <https://doi.org/10.1190/geo2019-0058.1>, 2019.

952 Haskell, N. A.: The dispersion of surface waves on multilayered media, *Bull. Seismol. Soc. Am.*, 43, 17–34, 1953.

953 Herrmann, R. B.: Computer programs in seismology: an evolving tool for instruction and research, *Seism. Res. Lett.*,  
954 84, 1081–1088, <https://doi.org/10.1785/0220110096>, 2013.

955 Hofmeister, A. M.: Mantle values of thermal conductivity and the geotherm from phonon lifetimes, *Science*, 283, 1699–  
956 1706, <https://doi.org/10.1126/science.283.5409.1699>, 1999.

957 Irifune, T. and Tsuchiya, T.: Phase transitions and mineralogy of the lower mantle, in *Treatise on Geophysics*, Elsevier,  
958 pp. 33–60, <https://doi.org/10.1016/B978-0-444-53802-4.00030-0>, 2015.

959 Irifune, T.: Composition and structure of the Earth's mantle: a view from recent high-pressure mineral physics studies,  
960 *J. Mineral. Soc. Japan*, 19, 233–243, 1990.

961 Jackson, I., Fitz Gerald, J. D., Faul, U. H., and Tan, B. H.: Grain-size-sensitive seismic wave attenuation in  
962 polycrystalline olivine, *J. Geophys. Res.*, 107, 2360, <https://doi.org/10.1029/2001JB001225>, 2002.

963 Julià, J., Ammon, C. J., Herrmann, R. B., and Correig, A. M.: Joint inversion of receiver function and surface wave  
964 dispersion observations, *Geophys. J. Int.*, 143, 99–112, <https://doi.org/10.1046/j.1365-246X.2000.00217.x>, 2000.

965 Karato, S.-i. and Wu, P.: Rheology of the upper mantle: a synthesis, *Science*, 260, 771–778,  
966 <https://doi.org/10.1126/science.260.5109.771>, 1993.

- 967 Kausel, E. Some wave propagation modes from simple systems to layered soils, in Lai, C. G., and Wilmanski, K. (eds.),  
968 *Surface waves in geomechanics: direct and inverse modeling for soil and rocks*, Springer-Verlag, 165–202, 2005.
- 969 Kennett, B. L. N.: Seismic wave propagation in stratified media, ANU Press, <https://doi.org/10.2307/j.ctt24h2zr>, 2009.
- 970 Kennett, B. L. N. and Engdahl, E. R.: Travel times for global earthquake location and phase association, *Geophys. J.*  
971 *Int.*, 105, 429–465, <https://doi.org/10.1111/j.1365-246X.1991.tb06724.x>, 1991.
- 972 Haney, M. M. and Tsai, V. C.: Perturbational and nonperturbational inversion of Love-wave velocities, *Geophysics*, 85,  
973 F19–F26, <https://doi.org/10.1190/geo2019-0164.1>, 2020.
- 974 Huang, Z., Zhao, D., and Wang, L.: Seismic heterogeneity and mantle dynamics of the western Pacific subduction zone,  
975 *J. Geophys. Res. Solid Earth*, 116, B10303, <https://doi.org/10.1029/2011JB008401>, 2011.
- 976 Irifune, T., Isshiki, M., and Katayama, Y.: Iron partitioning and density changes of pyrolite in Earth's lower mantle,  
977 *Science*, 292, 1171–1173, <https://doi.org/10.1126/science.1057647>, 2001.
- 978 Jackson, I. and Faul, U. H.: Grain-size-sensitive viscoelastic relaxation in olivine: towards a robust laboratory-based  
979 model for seismological application, *Phys. Earth Planet. Int.*, 183, 151–163, <https://doi.org/10.1016/j.pepi.2010.09.005>,  
980 2010.
- 981 Jackson, M. G. and Dasgupta, R.: Compositional constraints on melting of Earth's heterogeneous mantle and  
982 implications for the generation of ocean island basalts, *Rev. Geophys.*, 56, 3–49,  
983 <https://doi.org/10.1002/2017RG000558>, 2018.
- 984 Karato, S.: On the origin of the asthenosphere, *Earth Planet. Sci. Lett.*, 321–322, 95–103,  
985 <https://doi.org/10.1016/j.epsl.2012.01.001>, 2012.
- 986 Kellogg, L. H., Hager, B. H., and van der Hilst, R. D.: Compositional stratification in the deep mantle, *Science*, 283,  
987 1881–1884, <https://doi.org/10.1126/science.283.5409.1881>, 1999.
- 988 Khan, A., Maclennan, J., and Connolly, J. A. D.: Inversion of seismic and geodetic data for the major element chemistry  
989 and temperature of the Earth's mantle, *Earth Planet. Sci. Lett.*, 284, 554–568,  
990 <https://doi.org/10.1016/j.epsl.2009.05.014>, 2009.
- 991 Khan, A., Cammarano, F., and Connolly, J. A. D.: Geophysical evidence for melt in the deep mantle, *Nature*, 455, 978–  
992 981, <https://doi.org/10.1038/nature07364>, 2008.
- 993 Kustowski, B., Ekström, G., and Dziewoński, A. M.: Anisotropic shear-wave velocity structure of the Earth's mantle: a  
994 global model, *J. Geophys. Res.*, 113, B06306, <https://doi.org/10.1029/2007JB005169>, 2008.
- 995 Lebedev, S. and van der Hilst, R. D.: Global upper-mantle tomography with the automated multimode inversion of  
996 surface and S-wave forms, *Geophys. J. Int.*, 173, 505–518, <https://doi.org/10.1111/j.1365-246X.2008.03721.x>, 2008.

Formatted: French

- 997 Lekic, V., Cottaar, S., Dziewoński, A., and Romanowicz, B.: Cluster analysis of global lower mantle tomography: a  
998 new class of structure and implications for chemical heterogeneity, *Earth Planet. Sci. Lett.*, 357–358, 68–77,  
999 <https://doi.org/10.1016/j.epsl.2012.09.014>, 2012.
- 1000 Matas, J., Bass, J. D., Ricard, Y., Mattern, E., and Bukowski, M. S. T.: On the bulk composition of the lower mantle:  
1001 predictions and limitations from generalized inversion of radial seismic profiles, *Geophys. J. Int.*, 160, 973–990,  
1002 <https://doi.org/10.1111/j.1365-246X.2005.02526.x>, 2005.
- 1003 Montagner, J. P. and Kennett, B. L. N.: How to reconcile body-wave and normal-mode reference Earth models,  
1004 *Geophys. J. Int.*, 125, 229–248, <https://doi.org/10.1111/j.1365-246X.1996.tb06548.x>, 1996.
- 1005 Murakami, M., Hirose, K., Kawamura, K., Sata, N., and Ohishi, Y.: Post-perovskite phase transition in MgSiO<sub>3</sub>,  
1006 *Science*, 304, 855–858, <https://doi.org/10.1126/science.1095932>, 2004.
- 1007 Nolet, G., Montelli, R., Dahlen, F. A., Masters, G., Engdahl, E. R., and Hung, S. H.: Seismic evidence for a deep mantle  
1008 thermal anomaly in the mantle beneath East Africa, *Geophys. Res. Lett.*, 31, L20607,  
1009 <https://doi.org/10.1029/2004GL020572>, 2004.
- 1010 Ritsema, J., Deuss, A., van Heijst, H. J., and Woodhouse, J. H.: S40RTS: a degree-40 shear-velocity model for the  
1011 mantle from new Rayleigh wave dispersion, teleseismic traveltimes and normal-mode splitting function measurements,  
1012 *Geophys. J. Int.*, 184, 1223–1236, <https://doi.org/10.1111/j.1365-246X.2010.04884.x>, 2011.
- 1013 Rudolph, M. L., Lekic, V., and Lithgow-Bertelloni, C.: Viscosity jump in Earth's mid-mantle, *Science*, 350, 1349–  
1014 1352, <https://doi.org/10.1126/science.aad1929>, 2015.
- 1015 Simmons, N. A., Forte, A. M., and Grand, S. P.: Thermochemical structure and dynamics of the African superplume,  
1016 *Geophys. Res. Lett.*, 34, L02301, <https://doi.org/10.1029/2006GL028009>, 2007.
- 1017 Stixrude, L. and Lithgow-Bertelloni, C.: Thermodynamics of mantle minerals – I. Physical properties, *Geophys. J. Int.*,  
1018 162, 610–632, <https://doi.org/10.1111/j.1365-246X.2005.02642.x>, 2005.
- 1019 Stixrude, L. and Lithgow-Bertelloni, C.: Thermodynamics of mantle minerals – II. Phase equilibria, *Geophys. J. Int.*,  
1020 184, 1180–1213, <https://doi.org/10.1111/j.1365-246X.2010.04890.x>, 2011.
- 1021 Takei, Y.: Effect of pore geometry on Vp/Vs: From equilibrium geometry to crack, *J. Geophys. Res. Solid Earth*, 107,  
1022 ECV 6-1–ECV 6-12, <https://doi.org/10.1029/2001JB000522>, 2002.
- 1023 Tsuchiya, T., Tsuchiya, J., Umemoto, K., and Wentzcovitch, R. M.: Phase transition in MgSiO<sub>3</sub> perovskite in the  
1024 Earth's lower mantle, *Earth Planet. Sci. Lett.*, 224, 241–248, <https://doi.org/10.1016/j.epsl.2004.05.017>, 2004.
- 1025 van der Hilst, R. D., Widiyantoro, S., and Engdahl, E. R.: Evidence for deep mantle circulation from global  
1026 tomography, *Nature*, 386, 578–584, <https://doi.org/10.1038/386578a0>, 1997.

1027 Walter, M. J., Kohn, S. C., Araujo, D., Bulanova, G. P., Smith, C. B., Gaillou, E., Wang, J., Steele, A., and Shirey, S. B.:  
1028 Deep mantle cycling of oceanic crust: evidence from diamonds and their mineral inclusions, *Science*, 334, 54–57,  
1029 <https://doi.org/10.1126/science.1209300>, 2011.